THE DETECTABILITY OF TRANSIT SIGNALS FROM A MICROLENSED SOURCE STAR WITH EUCLID

A thesis submitted to the University of Manchester
for the degree of Master of Philosophy
in the Faculty of Engineering and Physical Sciences

2014

By
Yun-Hak Kim
School of Physics and Astronomy

Contents

List of Tables

List of Figures

Abstract

Since the middle of the 1990's, surveys into exoplanets have started to blossom and the interst into this area has been increasing. There are several space missions with the main aim of detecting exoplanets and future missions are anticipated. Ground-based observatories also carry out surveys into exoplanets very actively. Upcoming microlensing survey such as 'KMTNet (Korea Micro-lensing Telescope Network)' could contribute considerably by observing thousands stars in the Galactic bulge with a high observational frequency (Kim et al., 2010). In addition to this, one of the ESA's upcoming space mission called 'Euclid' is aslo expected to contribute to the area of exoplanet detection through microlensing technique despite the fact that Euclid's main goal is to study dark energy. Advancements in detector technologies and analysis techniques will open up a new era of stuyding exoplanets by gravitational microlensing for example, assisting in making more informative 'exoplanet demography' (Penny et al., 2013). Furthermore, transit surveys are a very active research, particularly with legacy missions such as 'Kepler' and 'CoRoT'. Apart from this, ground-based surveys have been also active by such as 'MEarth' and 'HATNet (Hungarian-made Automated Telescope)'.

In this dissertation, the detectability of transit signals of exoplanets orbiting around a source star is investigated with Euclid's photometry. The basic concept of this simulation is that when a source star, which is generally faint is magnified by microlensing effect, some transit signals of exoplanet orbiting around a source star can be detected. 9311 source stars were generated based on the Besançon Galactic model and simulated. We also generated exoplanet properties such as mass, radius, period, host separation and etc based on a Keplerian orbit assuming that every source star has only one exoplanet. As a next step, we set several selection conditions in terms of signal-to-noise ratio (SNR), orbital period and period precision between generated period and fitted period. When it comes to the SNR selection condition, we set a threshold of 50, which corresponds to a 2% uncertainty. Orbital period is also set as a maximum 10 days for the confirmation of transit signals from the observation duration (30 days) of our scenario. We also set a cutline for the period precision within 1%. More detailed information and procedures are described in the following sections. The main result is that we can achieve a 18% detectability with Euclid. This value may change when limb darkening and orbit eccentricity effects are considered. Furthermore, since only a single source star with one exoplanet orbiting was investigated in this disseration, there will be also some changes in the result if binary or multiple systems are considered.

University of Manchester,
Yun-Hak Kim

Master of Philosophy
The detectability of transit signals from a microlensed source star with *Euclid*
23 September 2014

Declaration

No portion of the work referred to in the thesis has been submitted in support of an application for another degree or qualification of this or any other university or other institute of learning.

Copyright

Acknowledgements

This dissertation could have not been written without the support, encouragement and guidance of several people. First of all, I would like to be extremely grateful to my supervisor, Dr. Eamonn Kerins who supported and guided me actively and continuously for the success of finishing this dissertaion. He suggested this interesting and valuable project to me in November, 2012 and he gave the continual intellecture support for this project and personal encouragement whenever I suffered from the research and even personal problems throughout two years of my Master of Philosophy degree.

I sincerely appreciate to my colleague, Supachai Awiphan. He helped me to become accustomed to many basic things such as programme language with regard to this dissertation. My gratitude is naturally extended to course director Dr. Clive Dickinson, co-supervisor Dr. Neal Jackson and advisor Prof. Richard Battye for their support during this study. I also would like to express my appreciation to all JBCA staffs and postgraduate students who were very friendly and helpful.

I also really appreciate to Prof. Yi and Prof. Hui, my ex-supervisors at the Chungnam National University, Republic of Korea who helped and advised me to study at the University of Manchester, United Kingdom.

I would like to extend my grateful mind to my beloved family in Republic of Korea. They supported me physically and spiritually during this study. Without their support, this study would not have been even possible.

Finally, I would like to express my appreciation to everybody who was helpful and supportive for the success of this dissertation and, I apologize to whom I could not mention one by one personally.

The Author

The author was born in Republic of Korea and graduated with a Bachelor of Science in Astronomy from Chung Nam National University, Republic of Korea, in 2011. After his undergraduate period, he started studying for a M.Phil (Astronomy and Astrophysics) in September 2012 at the University of Manchester. The research aspects of which are presented in dissertation. The authors future career plan has not decided yet but, he has been considering as many possibilities as he can take.

Chapter 1

Introduction

Nowadays, exoplanet research has become one of the most active areas in astronomy. As a result, more than 1700 confirmed exoplanets have been discovered through several detection methods such as transit, gravitational microlensing, radial velocity and so on (Perryman, 2011). We have learnt that, unlike our solar system, planets can orbit around dwarfs, giants, or even neutron stars. In addition to this, we also have learnt that exoplanet properties also vary widely. With advances in technology, especially with the possible advent of space-based microlensing, it should become possible to prove rare and exotic exoplanet systems such as a transit signal from a microlensed source. Such exotic events would enable us to find transiting systems at potentially much greater distances than at present.

In this work, the detectability of an exoplanet transit signal from a microlensed source star is assessed with Euclid's photometry. In the remainder of this Chapter, the historical background of exoplanets and the detection methods will be described. In Chapter 2, two detection techniques (microlensing and transit), which will form the focus of this thesis, will be described in more detail. The procedures of generating simulations with Euclid's photometry is provided in Chapter 3 and the results are presented in Chapter 4. Finally, in the last Chapter, the conclusions will be presented and possible avenues for further research discussed.

1.1 Historical background

An exoplanet is a planet which is outside of our Solar System. Conventionally, we think of exoplanets as being bound to other host stars and this thesis focuses on this case. However, exoplanets may also exist which are unbound to any star and these are referred to as a free floating planets (Sumi et al., 2011). After the discovery of the first exoplanet (PSR 1257+12) in 1992 through the pulsar timing method (Wolszczan & Frail, 1992), the interest in exoplanets has increased significantly. More than 1700 confirmed exoplanets have been detected by both space missions and ground-based surveys down to around the Earth size. After the launch of the Kepler space telescope in 2009 by NASA, the number of exoplanet candidates has increased rapidly (Batalha et al., 2013).

Following the first discovery in 1992, several different methods such as transit, radial velocity, gravitational microlensing and direct imaging have been developed and used to discover exoplanets. These detection methods have their own strong points and weak points.

Exoplanets are generally classified by distance and size. When it comes to distance from a host star, exoplanets are termed 'hot planets' or 'cold planets'. Hot planets are generally defined as planets orbiting inside of the snow line. The snow line refers to a particular distance from the host star where it is cool enough to form hydrogen compounds such as water, ammonia, and methane to condense into solid ice grains. According to (Ida & Lin, 2005), when the protostar reaches to main-sequence star, the luminosity becomes an important factor and the distance of the snowline (a_{snowline}) is proportional to $M_\star^2$. Here, $M_\star$ is a star's mass. However, due to more consideration about other factors (Kennedy & Kenyon, 2008), the temperature at the snow line is estimated to be about 170 K and is generally written as

$$a_{\mathrm{snowline}}(\mathrm{AU}) = 2.7\left(\frac{M_\star}{M_\odot}\right). \quad (1.1)$$

Cold exoplanets orbit outside of the snow line. The snow line plays an important role in planet formation theory. In the core accretion model (Bodenheimer & Pollack, 1986), planets beyond of the snow line can form with larger cores due to the presences of solid hydrogen compounds. Their large cores can accrete much more of the surrounding gas to form gas giant planets (Hubickyj et al., 2004). When it comes to size, exoplanets can be classified by five categories: 'Earth-size ($1.25 < R_\oplus$)', 'Super-Earth-size ($1.25 - 2R_\oplus$)', 'Neptune-size ($2 - 6R_\oplus$)', 'Jupiter-size ($6 - 15R_\oplus$)' and, 'larger-size', which is larger than Jupiter-size ($15 > R_\oplus$)[1].

1.2 Detection methods

1.2.1 Methods for detecting hot exoplanets

Radial Velocity

Exoplanets can induce periodic perturbations of the star due to the motion of the orbiting planet. This perturbation produces a host star reflex velocity with an amplitude K, due to a planet of mass M_p, which can be expressed as (Cumming et al., 1999)

$$K = \left(\frac{2\pi G}{P}\right)^{1/3} \frac{M_p \sin i}{(M_p + M_\star)^{2/3}} \frac{1}{\sqrt{1-e^2}}, \tag{1.2}$$

where P is the planet's orbital period, i is the planet's orbital inclination and e is the eccentricity of the planet's orbit. It can be seen from the equation, this technique is suitable for massive and short period planets orbiting close to the host star. However, radial velocity can not determine the mass precisely due to the uncertainty of the orbital inclination i. Hence, radial velocity measurements provide only a lower mass $M_p \sin i$. However, radial velocity provides an accurate determination of the period (Perryman, 2011).

The first radial velocity signal was published by Cambell et al. (1988) with γ Cep A (see Figure 1.1). However, they were unable to confirm at the time that the signal

[1] http://www.nasa.gov/mission_pages/kepler/news/kepler-461-new-candidates.html#.VARrCvHxXy0

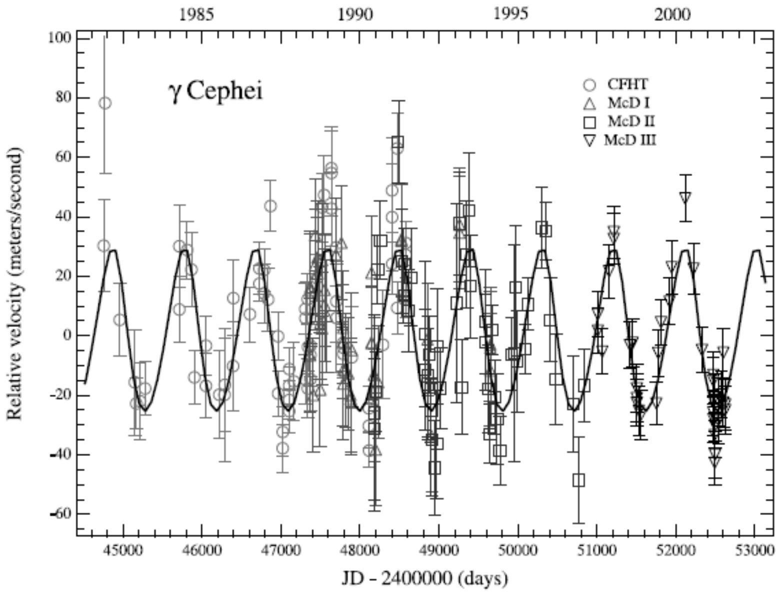

Figure 1.1: Orbital radial velocity data for the exoplanet γ Cep A, together with the best fit radial velocity solution (solid line). The data are from CFHT (Canada-France-Hawaii Telescope), MCD I (McDonald Observatory Planetary Search (MOPS) phase I), MCD II (MOPS phase II), and MCD III (MOPS phase III) respectively (Hatzes et al., 2003).

was due to an exoplanet. The first confirmed detection came from observations of 51 Peg (Mayor & Queloz, 1995). Through continued technical and theoretical advances, there are now more than 500 exoplanets which have been discovered by the radial velocity method so far[2].

The radial velocity technique has discovered several interesting cases. Firstly, a single star υ Andromedae was found for the first time as having a multiple planet system, consisting of 3 planets (Butler et al., 1999). Secondly, with remarkable improvement of radial velocity accuracy, lower mass planets that correspond to Super-Earth size are starting to be discovered. HD 69830 (a triple Neptune system) (Alibert et al., 2006), GJ 581 (five or six-planet system) (Bonfils et al., 2005) are examples. Other than that, the radial velocity method has discovered planets around binary and multiple stars systems (e.g γ Cep, binary system) (Perryman, 2011).

The transit method

When a planet passes across its host star, we can observe it as a transit. However,

[2]http://www.exoplanet.eu/

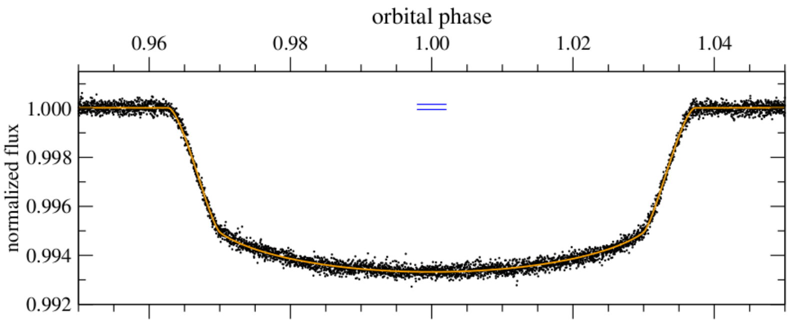

Figure 1.2: The Kepler transit light curve of HAT-P-7 (Welsh et al., 2010).

since the system is too far from the observer to resolve the star, the star light constitutes a point source and we observe a subtle decrease in the light curve of the star.

The trigger condition for a transit is expressed as

$$r(t_c)\cos i \leq R_\star + R_p, \tag{1.3}$$

where $r(t_c)$ is the distance of the planet from the host star at the time of mid-transit t_c, and $R_\star$ and R_p are the radii of the star and planet, respectively. In general, transit light curve of single exoplanet looks like as Figure 1.2.

As this detection technique totally depends on the transit probability, it is favorable for planets orbiting close to their host star and also planets with large radius (generally these are high mass planets). Large planets cut out more of the host star's light producing a deeper transit. The depth of the transit is given by the ratio of the area of the planet to that of the host star.

Since the first exoplanet was discovered by the transit method in 1999 (Queloz et al., 2000), many surveys have been conducted and are ongoing. Two space missions have been flown: CoRoT, which was launched in 2006 and decommissioned in January 2014 (Bakos et al., 2011); and Kepler, which was launched in 2009 (Borucki et al., 2010b).

Space-based transit surveys enable the discovery of Earth-like planets orbiting within the habitable zone of Sun-like host stars. Due to one of the characteristics of the transit effect, planets are mainly detected close to the host star. Therefore, in order to increase detectability of habitable planets, surveys can focus on lower mass stars (e.g. K or M type). Their habitable zones lie at roughly 0.1 AU∼0.4AU which, is more favorable for detection through the transit method (Sipőcz et al., 2013).

Another important role of transit detections is to confirm planets that have already been detected by radial velocity (e.g. HD 189733 b, Bouchy et al., 2005). Since, $\sin\, i \simeq 1$ for a transit to occur, the radial velocity measurment $M_p \sin\, i \simeq M_p$ and so we obtain the mass of the planet directly. Moreover, the transit data also provides the size of the planet, assuming we know the size of the host star. As a result, transit and radial velocity data together give the density of the planet. Transit surveys have found hundreds of planetary systems including dozens of multiple planet systems which are listed[3]. We develop the theory of the transit method futher in Chapter 2.

1.2.2 Methods for detecting cold exoplanets

Gravitational microlensing

According to the Einstein's general relativity, the presence of matter distorts spacetime, and hence, when light rays pass this distorted region, the path of the light will be deflected as a result. Due to this, the light from the background star is magnified at around lensing star. This effect is called gravitational lensing. A special case of gravitational lensing occurs within our Galaxy, which is referred to as microlensing (Paczynski, 1996a). Stars or planets can gravitationally lens background stars but, the image distortion is too small to observe (of the order of milliarcseconds). Instead, the signal varies with time over a typical range from days to years. Microlensing events are rare with typically one occurance per few million background stars. As discussed in Chapter 2, current surveys detect around two thousand events per year. The vast majority of microlensing signals come from stars microlensing each other. In less than 1% of cases, there is a evidence that the lens has a planetary companion. Together the planet and the host star act as a

[3]http://www.exoplanet.eu/

multiple lens system (Perryman, 2011). The multiple lens system can produce more than two images of the source resulting in burst of magnification as these images appear or disappear. The domain where significant spacetime distortion occurs can be expressed as the 'Einstein Radius' and its angular radius (θ_E), which is given by

$$\theta_E \equiv \left(\frac{4GM_{Lens}}{c^2 D_{\mathrm{rel}}} \right)^{1/2}. \tag{1.4}$$

where, $D_{rel}^{-1} = D_l^{-1} - D_s^{-1}$, D_s and D_l are distances from the observer to the source and lensing star, respectively.The physical radius R_E can be expressed by multiplying by the distance to the lens (Paczynski, 1996a)

$$R_E \equiv \theta_E D_l = \left(\frac{4GM_{Lens} D_l^2}{c^2 D_{\mathrm{rel}}} \right)^{1/2}, \tag{1.5}$$

where, G is the gravitational constant, M_{Lens} is the lensing star's mass. If there is a planet orbiting the lensing star, there will be an additional change in magnification (Mao & Paczynski, 1991). Since 2004, when the first exoplanet was discovered using microlensing, OGLE-2003-BLG-235 (Bond et al., 2004b), more than 30 exoplanets have been discovered[4].

Microlensing theory is developed further in Chapter 2.

Direct imaging

Direct imaging refers to obtaining an actual image of an exoplanet. There are two possibilities: an image can be observed from the reflected light from the host star (visible light); or from the thermal emission from the planet's own internal energy (typically observable in the infrared). However, there are difficult challenges to direct detection. There are two important parameters that determine the difficulty of detection: the flux ratio of planet to star; and the angular separation of the planet from the host star. When it comes to the angular separation, it can be expressed as

$$\Delta\theta = 1 arcsec \left(\frac{r_\perp}{AU} \right) \left(\frac{d}{pc} \right)^{-1}, \tag{1.6}$$

[4] http://www.exoplanet.eu/

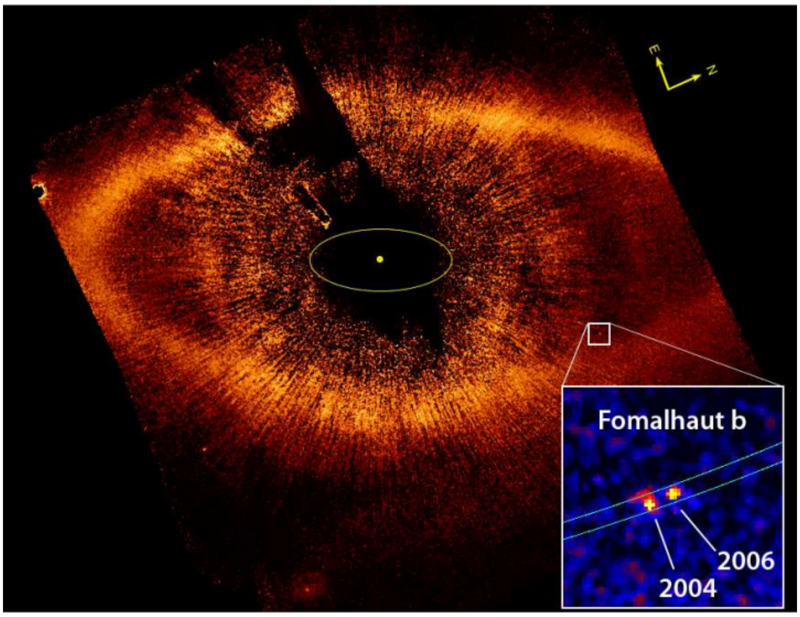

Figure 1.3: A Hubble Space Telescope (HST) coronagraphic direct image of Formalhaut and an exoplanet in the system Formalhaut b (within the square) (Kalas et al., 2008).

where $r_{\perp}$ is the projected separation and d is the distance from the observer.

Since the first discovery of exoplanets by the direct imaging method (2M1207b) (European Southern Observatory, 2005) surveys are now onging using ground-based observatories. Over the next decade, new large telescope facilities such as the European Extremely Large Telescope (E-ELT) (Marchiori et al., 2012), the Giant Magellan Telescope (GMT) (Johns, 2008), and the Thirty Metre Telescope (TMT) (Crampton et al., 2009) will exploit this method to detect lower mass planets. Figure 1.3 shows an example of direct image of exoplanet.

1.2.3 Other methods

Pulsar timing

A planet orbiting its host star can produce the periodic oscillation of the position of the barycentre of a planet-star system. This phenomenon can be recognisable by measuring the radial velocity and astrometric position of the star. This oscillation has an amplitude expressed as

$$\tau_p = \left(\frac{1}{c}\right)\left(\frac{a_p \sin i M_p}{M_\star}\right), \tag{1.7}$$

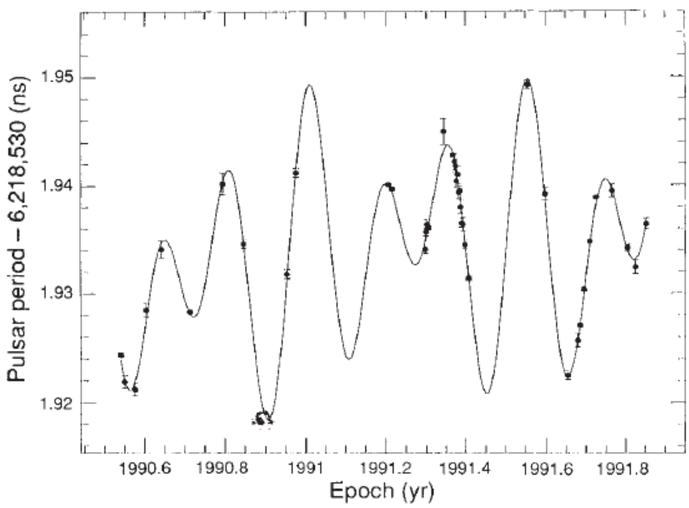

Figure 1.4: Period varaiations of PSR1257 +12. The solid line indicates changes in period predicted by a two-planet model of the system (Wolszczan & Frail, 1992).

where c is the speed of light and a_p is the distance from the barycentre to the planet. Millisecond pulsars have very accurate periods as determined by timing. There are around 1700 known pulsars including in excess of 80 milliarcsecond pulsars. Pulsar timing allows orbiting astronomical bodies to be detected (Wolszczan & Frail, 1992). The first planet discovered through timing was PSR B1257+12 (see Figure 1.4), a 6.2 milli-second period pulsar at 300 pc distance. At least two terrestrial-mass companinons were indicated from the timing residuals with masses of $M \sin i \simeq 2.8$ and $3.4M_\oplus$ (Wolszczan & Frail, 1992). There are more than 10 confirmed pulsar exoplanets so far[5], amongst them, HW Vir (Lee et al., 2009), DP Leo (Qian et al., 2010), and NN Ser (Beuermann et al., 2010).

Astrometry

This technique is closely related to the radial velocity method and involves detecting the shift in the position in the sky of a host star in response to the gravitational pull of an orbiting planet. Present accuracy can detect 1 milli-arcsec shifts with Hipparcos and the HST-Fine Guidance Sensors. This accuracy will be greatly improved with ESA's Gaia satellite (de Bruijne, 2012). The route of a star orbiting the star-planet barycentric comes into view projected on the plane of the sky as an

[5] http://www.exoplanet.eu/

ellipse having angular semi-major axis α given by

$$\alpha = \frac{M_p}{M_\star + M_p} a \simeq \frac{M_p}{M_\star} a \equiv \left(\frac{M_p}{M_\star}\right)\left(\frac{a}{1AU}\right)\left(\frac{1pc}{d}\right) arcsec, \tag{1.8}$$

where a is the semi-major axis of the planet orbit for an assumed circular shape, d is the distance from the observer. Since α is proportional to both M_p and a, and inversely to d, astrometry is particularly sensitive to high mass and long orbital period planets (Perryman, 2011).

Currently, there are only two confirmed astrometric detections of exoplanets. After the Hipparcos satellite operated successfully (1989-93), as a successor of Hipparcos, the Gaia space mission was launched in December 2013 (Sozzetti, 2014). During its five year mission lifetime, Gaia should discover thousands of giant planets with semi-major axis $a = 3 - 4$ AU out to 200 pc, and should succeed in characterising hundreds of multi-planet systems (Perryman, 2011).

Chapter 2

The transit and microlensing techniques

The aim of this thesis is to test whether transit signals due to an exoplanet orbiting a microlensed source star is likely to be detected with future space-based surveys. The underlying theories behind the microlensing and transit techniques is therefore explored in more detail in this chapter. This theory forms the basis for the simulation work in the following chapter.

2.1 Transit

The transit effect can be described as a decrease in flux when a planet crosses in front of the host star. From Figure 2.1, the distance between the star and planet can be expressed as

$$r = \frac{A(1 - e^2)}{1 + e\ cos f}, \tag{2.1}$$

where A is the semi-major axis between the host star and planet, and $f = \theta - \varpi$ is referred as the true anomaly shown in Figure 2.1. True anomaly is an angular parameter that defines the position of a celestial body moving along a Keplerian orbit. It is described as the angle between the direction of periapsis and the current position of the celestial body.

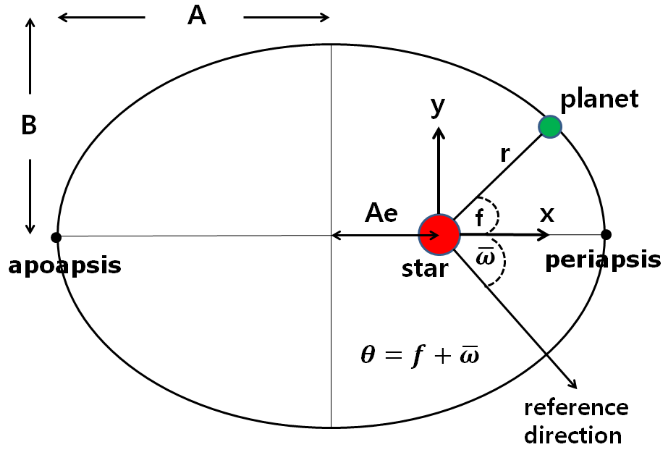

Figure 2.1: The geometry of ellipse-shape trajectory. A refers to the 'semi-major axis' and B indicates the 'semi-minor axis'. e is the 'eccentricity' of the trajectory and ϖ is referred as the 'longitude of periapse'.

The observed flux changes with time t during the transit, with the combined flux $F(t)$, which includes both star and planet flux, given by

$$F(t) = F_\star(t) + F_{\text{planet}}(t) - \begin{cases} p^2\ \alpha_{\text{tra}}(t) & \text{transits,} \\ 0 & \text{outside eclipses,} \\ \alpha_{\text{occ}}(t)\ F_{\text{planet}}(t) & \text{occultations (i.e. secondary transit),} \end{cases} \tag{2.2}$$

where $F_\star$ and F_{planet} are the fluxes from the star and planet and p is the radius ratio between planet and star ($R_{\text{planet}}/R_\star$). When it comes to the flux from the planet, we refer to the reflected light that comes from the star, neglecting any internal energy source. The dimensionless factor α represents the overlap area (fractional value from 0 to 1) between the star and the planet. The specific forms for α are given in Section 3.3. If we assume that I_p and $I_\star$ are the averaged intensities of the planet and star, respectively, then the maximum loss of light δ can be expressed as

$$\delta_{\text{tra}} \approx p^2 \left[1 - \frac{I_p(t_{\text{tra}})}{I_\star}\right], \tag{2.3}$$

where t_{tra} is the time of mid-transit.

In the usual case, the light from the planet is negligible. Therefore, $\delta_{\text{tra}} \approx p^2$. For the secondary transit, we have (e.g. Murray & Correia, 2011),

$$\delta_{\text{occ}} \approx p^2 \frac{I_p(t_{\text{occ}})}{I_\star}. \tag{2.4}$$

2.2 Transit surveys

2.2.1 Ground-based surveys

Transit surveys from the ground have been ongoing since before 1999 and from space since the launch of the CoRoT mission in 2006. There are many ground-based surveys; here we dicuss two examples.

The **Wide Angle Search for Planets** (WASP, now SuperWASP) project has been operating since 2000. This project has two observational sites. One is located at the Observatorio del Roque de los Muchachos on La Palma using a telescope equipped with multiple wide-angle cameras. Another clone facility is also located at the Sutherland Station of the South African Astronomical Observatory (SAAO). At each observatory, there are eight 200 mm camera lenses (0.11 m aperture) (Smith & WASP Consortium, 2014) and, these telescopes have a field-of-view of 7.8×7.8 squared degrees with an angular scale of 13.7 arcsecond per pixel and a photometric precision of better than 1% for objects with a magnitude between 7.0 and 11.5 of V-band (Pollacco et al., 2006). Except for the galactic plane region, they observe a dozen fields of the sky per night with a 10 minutes typical cadence (Smith & WASP Consortium, 2014). Their first public data release was in 2010 based on 3,631,972 raw images and 17,970,937 light curves which were obtained between 2004-2008 (Butters et al., 2010). There are several scientific discoveries such as WASP-12b (amenable system to probe the planet's atmosphere) (Sing et al., 2013) and WASP-17b (the first known retrograde direction orbiting exoplanet which plays a key role in studying the formation and evolution of hot Jupiters) (Anderson et al., 2010).

The **Hungarian Automated Telescope Network** (HATNet) project comprises a newtwork of six telescopes. Four telescopes are located at Whipple Observatory, Arizona and the others are located at Mauna Kea observatory, Hawaii. Another enhancement project which is called HAT-South has also been operational since 2009 (Bakos, 2011). It has a network system of six identical telescopes and these are established at three locations (two each at Las Campanas in Chile, Siding Springs in Australia and High Energy Stereoscopic System in Nambia). This project has almost 24 hour coverage and is also able to detect long period transits up to 20 days. HATNet has discovered roughly 50 exoplanets so far through the transit method[1].

2.2.2 Space missions

The space mission **CoRoT** (COnvection ROtation and planetary Transits) was launched in 2006 with goals of stellar seismology and searching for exoplanets. The project was led by CNES (French Space Agency) in conjunction with ESA (European Space Agency). The camera has 2.7×3.05 degrees field-of-view with the four CCDs (AS CCDs, PF CCDs). Their targets are R-band magnitudes between 11.5 and 16 and V-band magnitudes between 5.4 and 9.2 (Auvergne et al., 2009). However, it was retired in 2013 due to system failure[2]. Until its retirement, CoRot had discovered approximately 30 transiting exoplanets including the first super-Earth CoRoT-7b (Léger et al., 2009), CoRoT-3b (much heavier exoplanet than Jupiter) (Deleuil et al., 2008).

The **Kepler** space mission was launched in 2009 having a goal of determining the frequency of Earth-sized exoplanets inside of and near the habitable zone of Sun-like stars (Borucki et al., 2010a). The telescope of this mission was designed with a 0.95 m aperture and 42 CCDs (105 square degrees). They used Kepler's normal list of 156,097 exoplanet target stars with the Kepler K_p bandpass, which covers both the V and R bandpass. Most stars were included in the range of between $9 < k_p < 16$ (Borucki et al., 2011a). In their initial results paper (Borucki et al., 2011b), the Kepler team reported 1235 planetary candidates from 998 extrasolar systems. The Kepler team initially designate their discoveries as exoplanet "candidates" until further data are able to unambiguously establish them as "confirmed" exoplanets. As

[1]http://www.exoplanet.eu/
[2]http://www.spacedaily.com/reports/Retirement_for_planet-hunting_space_probe_999.html

many of Kepler source stars are relatively faint, a large fraction of Kepler discoveries remain at candidate status. The characteristics of exoplanets discovered by Kepler mission are divided into five classes by size: 68 candidates of approximately Earth-size ($R_{planet} < 1.25R_{\oplus}$), 288 super-Earth-size ($1.25R_{\oplus} \leq R_{\rm planet} < 2R_{\oplus}$), 662 Neptune-size ($2R_{\oplus} \leq R_{\rm planet} < 6R_{\oplus}$), 165 Jupiter-size ($6R_{\oplus} \leq R_{\rm planet} < 15R_{\oplus}$), and 19 up to twice size of Jupiter ($15R_{\oplus} \leq R_{\rm planet} < 22R_{\oplus}$) (Borucki et al., 2011b). They have reported additional discoveries (Batalha, 2014) and, the number of confirmed exoplanets so far is roughly 1,000 among approximate 4,200 candidates[3].

The **PLATO** (PLAnetary Transit and Oscillations of stars) mission has recently been selected by ESA for their M3 launch opportunity between 2022 and 2024. Its instrument consists of 34 cameras with 12 cm diameter each (32 with 25 sec readout cadence and 2 with 2.5 sec candence) which will provide a 2232 square degree field-of-view and it will focus on bright stars (4-11mag) to detect and characterize exoplanets down to Earth-size by using the transit method. An asteroseismology survey will also be conducted for bright stars to obtain highly accurate stellar parameters such as masses and ages. PLATO is expected to observe up to one million stars and thousands of planets (Rauer et al., 2014).

2.3 Gravitational microlensing

2.3.1 Basic concept of single-lens microlensing

According to Einstein's conception, when the light passes close to a mass concentration, the light is bent by an angle

$$\alpha = \frac{4GM_{\rm lens}}{c^2 d}, \tag{2.5}$$

where $M_{\rm lens}$ is the lens star's mass and d is the closest distance between light ray and lens star (see Figure 2.2). The lens equation for an isolated point lens can be expressed as (e.g. Gaudi, 2012)

[3]http://kepler.nasa.gov/Mission/discoveries/

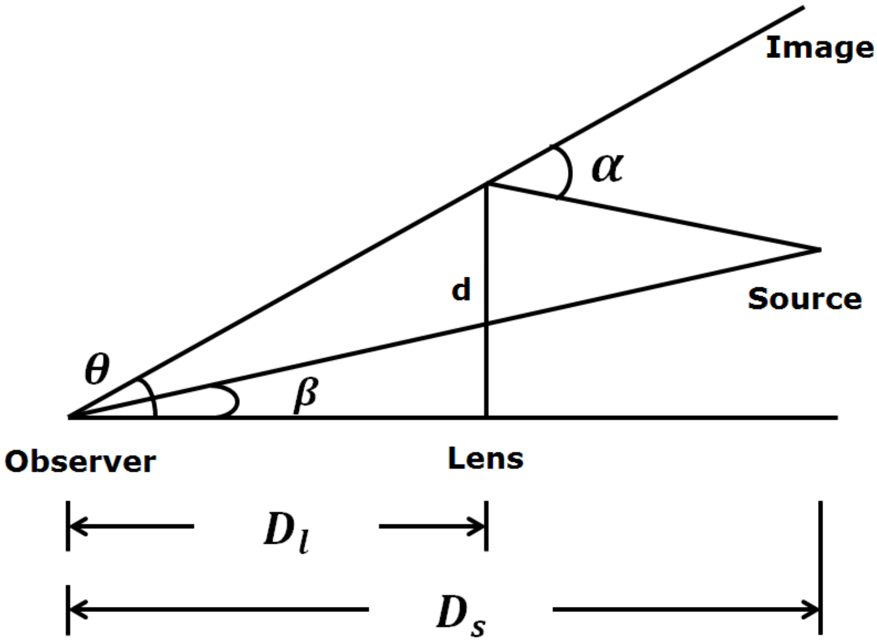

Figure 2.2: An exaggerated geometric picture of microlensing. The lensing star (Lens) is at a distance D_l and the source star (Source) is at a distance D_s from the Observer, repectively. θ is the angle between the image and lens, β is the angle between the lens and source star and, α is the deflection angle given by Equation 2.5 between image and source, respectively. For real microlensing cases, all angles are small enough to obey the small angle approximation.

$$\beta = \theta - \frac{4GM_{\mathrm{lens}}}{c^2 D_{rel}\, \theta}, \tag{2.6}$$

where $D_{rel}^{-1} = D_l^{-1} - D_s^{-1}$, D_l is the distance from the observer to the lensing star and D_s is the distance from the observer to the source (see Figure 2.2). When the lens and source are perfectly aligned ($\beta = 0$), this equation is equivalent to θ_E (see Equation 1.4).

2.3.2 Magnification

The magnification for each image is given by the ratio of the image area to the source area since surface brightness is conserved. If we normalize equation 2.6 by θ_E and then define $u = \beta/\theta_E$ and $y = \theta/\theta_E$, the equation becomes

$$u = y - y^{-1}, \tag{2.7}$$

and its quadratic solution in y is expressed as

$$y_{\pm} = \pm\frac{1}{2}(\sqrt{u^2+4} \pm u). \tag{2.8}$$

The ratio of the images to the source intensity can be expressed by the ratio of their areas by an amount of $y_{\pm}/u$. In addition to this, they will also be compressed by an amount of $dy_{\pm}/du$. Therefore, the magnification of each image can be expressed as

$$A_{\pm} = \left|\frac{y_{\pm}}{u}\frac{dy_{\pm}}{du}\right|. \tag{2.9}$$

Therefore, the total magnification can be calculated as

$$A(u) = A_{+} + A_{-} = \frac{u^2+2}{u\sqrt{u^2+4}}. \tag{2.10}$$

Note that when $u \ll 1$, $A(u) \simeq u^{-1}$ and the opposite case of $u \gg 1$, $A(u) \simeq 1+2/u^4$. For perfect observer-lens-source alignment ($u \to 0$), then the magnification becomes infinite theoretically ($A \to \infty$) but in practice is limited by the size of star (e.g. Gaudi, 2012). The highest magnification reported to date is $A \sim 3000$ in the case of OGLE-2004-BLG-343 (Dong et al., 2006b). In the case of a single-lens event in uniform motion, magnification can be changed by t_E, t_0 and t as

$$u(t) = \left(\left[\frac{t-t_0}{t_E}\right]^2 + u_0^2\right)^{1/2}. \tag{2.11}$$

Here, u_0 is the minimum impact parameter of the event, t_0 is the time of closest alignment when $u = u_0$ (maximum magnication), and t_E is the Einstein radius crossing time which can be expressed as,

$$t_E \equiv \frac{\theta_E}{\mu_{\rm rel}}. \tag{2.12}$$

Here, $\mu_{\rm rel}$ is the angular proper motion between the source and lens. Figure 2.3 is the visualized version of Equation 2.10 and 2.11.

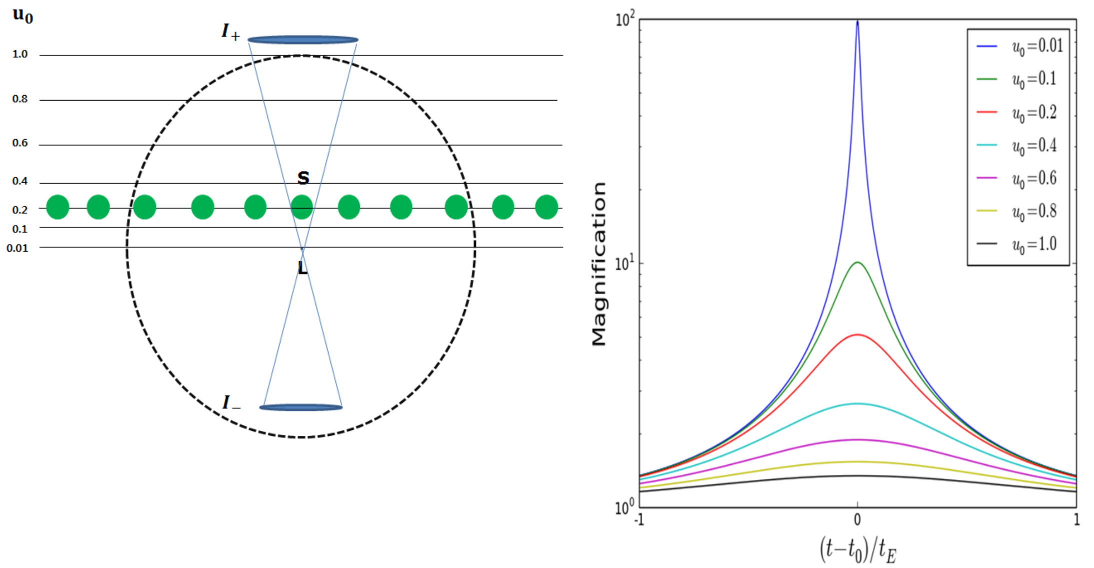

Figure 2.3: (left panel) The shown dashed circle implies angular Einstein radius θ_E. The green circle (S) is the source at an angular separation of $u_0 = \beta/\theta_E = 0.2$. we_+ and we_- are the two images created by microlensing effect. (right panel) The magnifications as a function of time for the seven trajectories which are introduced in left panel. The more u_0 goes to 1.0, the lower magnification is shown in right panel.

2.4 Microlensing surveys

2.4.1 Ground based: principle surveys

Since the early 1990s', several microlensing surveys have operated from ground-based observatories. Initially they focused on searches for MACHO dark matter (Jetzer, 1999) but later on turned their attention to searches for exoplanets.

The longest running microlensing survey is the Optical Gravitational Lensing Experiment **OGLE**. In 1992, when OGLE began, the original purpose of this survey was to discover dark matter through the microlensing effect toward the Magellanic Clouds and the Galactic Bulge. However, as a side benefit, OGLE has contributed to discoveries in extrasolar planets such as OGLE-2005-BLG-390Lb (first small and cold exoplanet, Ehrenreich et al., 2006). In the first phase OGLE-I (1992-1995) discovered the first microlensing event by a binary lens system (Udalski et al., 1994). After the first phase, they carried out two more phases OGLE-II(1996-2000) and OGLE-III(2001-2009). Since the fourth phase OGLE-IV(2010-present) OGLE data have contributed to the discovery of more than 30 exoplanets up to date[4].

OGLE has developed an Early Warning System (EWS) for detecting microlensing events (Udalski, 2003). The basic concept of this system is to compare the current brightness of a star with its mean brightness. When a star's brightness is observed as increased compared to its mean brightness, the star is marked and further analyzed for promising microlensing event candidate. This system has developed through various phases (OGLE-I to OGLE-III) to make it more efficient for microlensing. The Early Early Warning System (EEWS) is another OGLE-III system of data anyalysis in real time aiming through the deviations between the detection and the regular single mass microlensing light curve profile. The primary goal of EEWS is to provide the OGLE observer with fast information about microlensing events to enable rapid response from the observer. OGLE-III has distributed EEWS alerts via their EWS network to several microlensing follow-up groups (see following sub-section) to enable rapid-response observations.

Microlensing Observations in Astrophysics (MOA) is a collaborative project between New Zealand and Japan. They originally established a 61cm wide-field telescope at the Mt John Observatory in New Zealand and started the microlensing survey in 1995. The primary goal of this project was to detect dark matter, but is now focused towards exoplanets and stellar atmospheres (Yock et al., 2000). In 2005, a new 1.8-m telescope (MOA-II) was deployed with a much wider field-of-view of 2.2 square degrees (Sumi, 2010). In 2003, MOA data provided the first discovery of a microlensing exoplanet MOA 2003-BLG-53/OGLE 2003-BLG-235 (Bond et al., 2004a). Like OGLE, MOA data have contributed to the discovery of more than 30 exoplanets to date[5] thanks to the use of real time alert system.

The **Korea Microlensing Telescope Network** (KMTNet) is a new survey network that will focus on discovering earth-mass extrasolar planets using the microlensing technique. This project is designed to have 24-hour observational coverage by constructing three identical telescopes in three different time zones in the Southern Hemisphere (South Africa, Australia, and Chile). The telescope for this

[4]http://www.exoplanet.eu/
[5]http://www.exoplanet.eu/

project will be 1.6-m with a 2.0 square degrees field of view. The telescope will have observational coverage with a range between B-band (400 nm) and I-band (1000 nm). However, I-band will be the most important band for monitoring because it is less affected by extinction. They will also be sensitive to the stars with a magnitude between 13 and 20 toward Galactic bulge fields. KMTNet is expected to start operations in 2014 (Kim et al., 2010).

2.4.2 Ground based: follow-up surveys

The **Probing Lensing Anomalies Network** (PLANET) is one of the microlensing observation follow-up collaborations. The purpose of this survey is to conduct precise and frequent observations with multiple bands for microlensing events in progress to study potential exoplanet microlensing. They observe the sky with four 1-m class networked optical telescopes located at four places each in the southern hemisphere: South Africa Astronomical Observatory (SAAO); Cerro Tololo Inter-American Observatory (CTIO); Canopus Observatory; and Perth Observatory (Dominik et al., 2002). Through the continuous collaboration work with such as OGLE and MOA, they contributed to the discovery of several extrasolar planets by using the microlensing effect such as OGLE-2005-BLG-071 (Udalski et al., 2005) and OGLE-2005-BLG-390 (Beaulieu et al., 2006).

Another follow-up survey **Microlensing Follow-Up Network** (μFUN) is an informal consortium consisting of amateur and professional observers who contribute to monitoring interesting microlensing events in the Galactic Bulge. The main goal of this survey is to observe high-magnification microlensing events which are able to provide the biggest chance to detect extra-solar planets orbiting the lensing star. They merged with PLANET in 2009[6] and now, observe the sky with a networked 23 telescopes to obtain more and precise data[7]. Their first high-magnification event discovery was OGLE-2005-BLG-071 ($A \sim 30$) (Udalski et al., 2005) and the highest magnification was OGLE-2005-BLG-343 ($A \sim 3000$) (Dong et al., 2006a).

[6]http://planet.iap.fr/

[7]http://www.astronomy.ohio-state.edu/ microfun/

2.4.3 Potential space missions: WFIRST and Euclid

There are two proposed space missions which are expected to launch after 2020 and will be capable of detecting exoplanets with microlensing.

The **WFIRST** (Wide-Field Infrared Survey Telescope) is a Hubble class NASA mission that is designed to detect exoplanets using microlensing and constrain dark energy using weak lensing. The exoplanet survey will take up 500 days among the 5 years life time. WFIRST is expected to discover apporoximately 3000 exoplanets around stars, 300 of which will be smaller than the Earth size as well as 2000 free oating planets, 200 of which will have a mass smaller than that of the Earth. WFIRST will be sensitive to determine the masses from 0.1 to 1000 Earth masses including exoplanets in the habitable zone (Barry et al., 2011).

Euclid is the second M-class mission of the cosmic version programme of the European Space Agency (ESA). The features of Euclid spacecraft can be seen from Figure 2.4. The mission's primary scientific goal is to constrain the nature of dark energy by measuring weak gravitaional lensing and galaxy clustering (Laureijs et al., 2014), but Euclid is also expected to carry out additional science. The launch date of this mission is anticipated in 2020 and is also expected to have 6-years lifetime. With a 1.2 metre telescope, Euclid will conduct a wide survey with 15,000 square degrees of extra-galactic sky and a deep survey with 40 square degrees of two ecliptic poles. The two instruments in the telescope are called as VIS and NISP. The visual instrument (VIS) camera is made of 36 CCDs in broad band (R+I+Z) which will be used for measuring the shapes of galaxies. The near-infrared instrument (NISP) camera is made of 16 HgCdTe near-infrared detectors with Y, J, and, H bands. It also has a eld of view of 0.55 square degrees and a resolution better than 0.3 arcseconds. Overall mission summary can be found in Figure 2.5. The **Exoplanet Euclid Legacy Survey** (ExELS) is one of the Euclid additional science proposals (Penny et al., 2013). ExELS is expected to conduct a microlensing survey toward the Galactic Centre to find exoplanets down to Earth mass with host separations from ~ 1 AU out to the free-floating (unbound) range for the first time. These cold and free-floating exoplanets should be a crucial discovery area for testing and

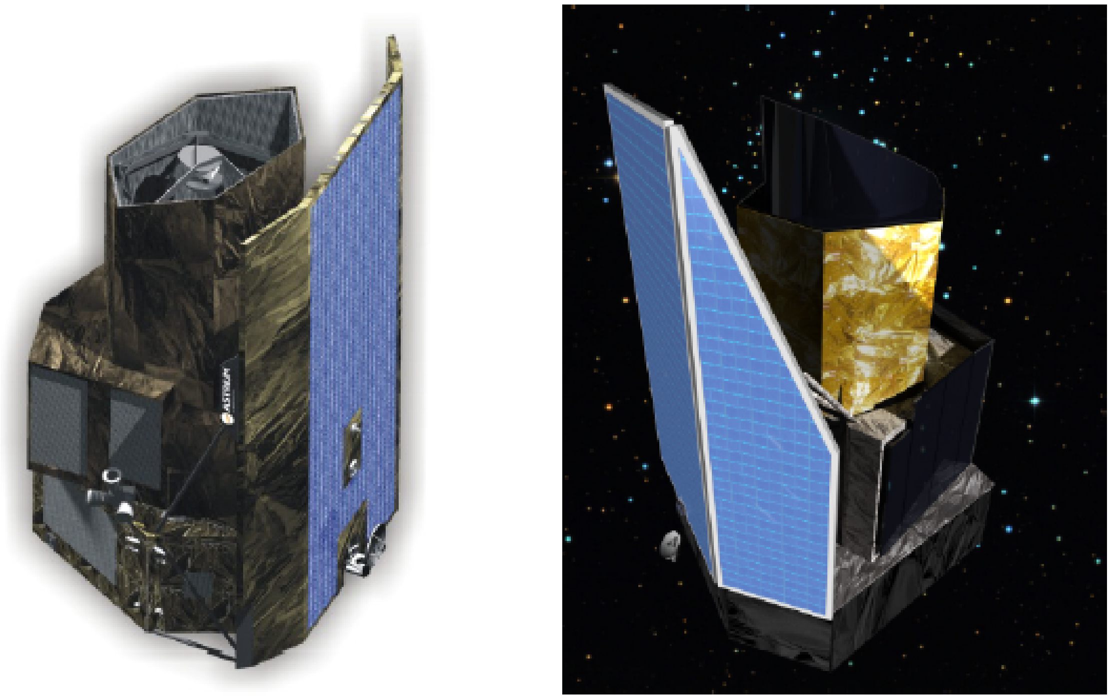

Figure 2.4: The design of the Euclid spacecraft. (left) designed by Astrium GmbH (Germany), (right) designed by Thales Alenia Space Italy (Turin) (Laureijs et al., 2012)

probing planet formation theories. ExELS mainly should detect a few hundred cold exoplanets around G, K, and M-type host stars, including ~ 45 Earth mass planets and ~ 6 Sub-Earth mass planets. Due to the design of Euclid's sun shield, Euclid's Solar aspect angle is determined as between 89 and 120 degrees, ExELS can possibly observe the Galactic bulge region for a maximum of one month duration, twice per year. ExELS will also be sensitive to hot exoplanets and sub-stellar astronomical objects through their transit signals. ExELS will use the gravitational microlensing technique and this will help detect around 1000 microlensing events per month in the region of 1.6 deg^2 of the Galactic bulge.

Euclid mission summary					
Main mission objectives					
Study the nature of dark energy and dark matter					
Surveys					
	Area (deg^2)	Description			
Wide survey	15,000 (required) 20,000 (goal)	Step and stare with 4 dither pointings per step			
Deep survey	40	In at least 2 patches of > 10 deg^2 2 magnitudes deeper than wide survey			
Payload					
Telescope	1.2 m Korsch, 3 mirror anastigmat, f=24.5 m				
Instrument	VIS	NISP			
Field-of-view	0.787 x 0.709 deg^2	0.763 x 0.722 deg^2			
Capability	Visual imaging	NIR imaging photometry			NIR spectroscopy
Wavelength range	550-900 nm	Y (920-1146 nm)	J (1146-1372 nm)	H (1372-2000 nm)	1100-2000 nm
Sensitivity	24.5 mag 10 σ extended source	24 mag 5 σ point source			3×10^{-16} erg $cm^{-2}s^{-1}$ 3.5 σ unresolved line flux
Detector technology	36 arrays 4k x 4k CCD	16 arrays 2k x 2k sensitive HgCdTe detectors			
Pixel size Spectral resolution	0.1 arcsec	0.3 arcsec			0.3 arcsec R=250
Spacecraft					
Launcher	Soyuz ST-2.1 B from Kourou				
Orbit	Large Sun-Earth Lagrange point 2 (SEL2), free insertion orbit				
Pointing	25 mas relative pointing error over one dither duration 30 arcsec absolute pointing error				
Observation mode	Step and stare, 4 dither frames per field VIS and NISP common FoV=0.54 deg^2				
Lifetime	7 years				
Operation	4 hours per day contact, more than one ground station to cope with seasonal visibility variations				

Figure 2.5: The overall summary of the Euclid space mission science and capabilities. The information is reproduced from (Laureijs et al., 2011).

Chapter 3

Microlensed transit signals with ExELS

We are interested in seeing whether ExELS is able to detect rare microlensing events such as transit signals from a microlensed source star. As mentioned in previous chapter, ExELS is one of the Euclid additional science proposals (see Section 2.4.3).We test this by running detailed simulations of microlensed transiting systems within an assumed Galactic model. In this Chapter, we adopt the Besançon Galactic model for our simulation and we consider Euclid's expected photometric performance to generate a source star catalogue. We also discuss how we generate microlensing events and exoplanet parameters for our simulation. In addition, we discribe the generation of realistic light curves with photometric errors and also the cuts we adopt for isolating transit signals from such events.

3.1 The Besançon Galactic model

The Besançon Galactic population synthesis model is basically designed to model galactic formation and evolution, stellar formation and evolution, stellar atmospheres and dynamical constraints from observed data so far. Four main stellar populations are modeled: the thin disc; the thick disc; the galactic bulge; and the stellar halo. Since the Galactic model is based on a theoretical background (for example stellar evolution, galactic evolution), the model is semi-empirical and is also constrained by observations (for example the local luminosity function and star counts). The disc scale height is constrained self-conistently by the calculated galactic potential. The star evolutionary track for their age (Haywood et al., 1997) is applied and standard parameters such as the initial mass function (IMF) and the star formation rate (SFR) is also included for the model computation. In addition, the observational errors can also be included in order to make it more realistic. Finally, Marshall et al. (2006) have modeled interstellar extinction distribution in three dimensions from the 2MASS survey (Cutri et al., 2003) in the inner Galaxy ($|l| \leq 100°$ and $|b| \leq 10°$), with 15 arcmin resolution. They calculated the extinction as a function of distance along a given line-of-sight by comparing observed reddened stars to unreddened simulated stars from The Besançon model. This distribution provides a realistic correction to the observed colours and magnitudes of the simulated stars.

3.1.1 The thin disc

The thin disc is a region which contributes significantly to the star counts towards the Galactic Centre. The disc is a double exponential distribution with a central hole. The scale height, scale length and size of the central hole are important parameters that are used to characterize the disc. A standard stellar evolution model is applied to generate the disc population which is based on a set of stellar evolutionary tracks, a constant SFR over 10 Gyr, and a broken power-law IMF which can be written as

$$\phi(M) = A \times M^{-\alpha}, \tag{3.1}$$

where A is a normalization constant, with the power-law index $\alpha = 1.6$ for $M < 1M_\odot$ and $\alpha = 3$ for $M > 1M_\odot$.

The density distribution of thin disc follows the Einasto (1979) law. According to Robin et al. (2003), the thin disc is divided into 7 age components ranging from

$0 \sim 0.15$ Gyr to $7 \sim 10$ Gyr. Except for the youngest population, whose age is less than 150 million years, the distribution of each disc is described by an axisymmetric ellipsoid with an axis ratio that depends on the age. The density law of the ellipsoid is given as

$$\rho_d = \rho_{d_0} \times \left[\exp\left(- \sqrt{0.25 + (\frac{a}{R_d})^2} \right) - \exp\left(- \sqrt{0.25 + (\frac{a}{R_h})^2} \right) \right], \tag{3.2}$$

where

$$a^2 = R^2 + \left(\frac{Z}{\epsilon} \right)^2, \tag{3.3}$$

with R and Z being cylindrical coordinates and ϵ is the axis ratio of the ellipsoid. The value of ϵ depends on age and can be found in the table 2 of Robin et al. (2003). In Equation 3.2, R_d is the scale length of the disc and R_h is the scale length of the inner hole. The density law is normalized by ρ_{d_0}, which is deduced from the local luminosity function (Jahreiß & Wielen, 1997) assuming that the Sun is located at $R_\odot = 8.5$ kpc from the Galactic Centre and $Z_\odot = 15$ pc from the Galactic plane.

3.1.2 The thick disc

The thick disc formation scenario is based on an assumption that it is formed by one or more merger events at the begining of the life of the thin disc. An age of 11 Gyr is adopted which is a little younger than the stellar halo and slightly older than the thin disc. The slight difference is 1 Gyr. They also adopted a thick disc metallicity of -0.78 dex and an IMF $\phi \propto M^{-0.5}$. More details about the parameters can be found in Robin et al. (2003).

3.1.3 The Galactic bulge

The Galactic bulge stellar population is assumed to have emerged from a single burst population with an age range of 6 and 10 Gyr. The IMF of this region has $\phi \propto M^{-2.35}$ for $M > 0.7\ M_\odot$ (Robin et al., 2003). Picaud & Robin (2004) carried out a comprehensive survey of the Galactic bulge stellar density and luminnosity function by fitting model parameters to a set of 94 windows in the bulge in the region $-8° < l < 10°$ and $-4° < b < 4°$ (Robin et al., 2012). A full description about the stellar density and the luminosity function can also be found in the same paper (Picaud & Robin, 2004).

3.1.4 The stellar halo

The stellar halo is basically an old and metal-poor region and is more extended than the bulge. Its origin is still not known but a homogeneous population of stars with a short period of star formation is assumed with an IMF $\phi \propto M^{-0.5}$. The halo is older than the bulge and is assumed as an age of 14 Gyr. The metalicity is also assumed as a metal poor (the mean Gaussian distribution [Fe/H] = -1.78) in this region (Robin et al., 2003). Due to the low local density similar to the thick disc, this region will marginally contribute to the microlensing event rate in our simulation.

3.2 Generating microlensing events

The first step to generate microlensing light curves are to specify four important key parameters which define how magnification evolves with time.

3.2.1 Generate parameters and conditions

The key parameters are: the impact parameter; the time of peak magnification; and the Einstein radius crossing time.

- The impact parameter u_0

u_0 is a parameter which indicates the highest magnification during the whole microlensing event, as discussed in Section 2.3. For detection, the magnification should be significantly more than 1. We adopt a minimum magnification of $3/\sqrt{5} = 1.34$, which corresponds to $u_0 = 1$ from Equation 2.10. Therefore, we set the maximum limit of $u_0 = 1$. For very small impact parameters, the finite size of the source star becomes important. This typically affects only a small fraction of microlensing events (Udalski, 2003) and so we ignore the finite source size effects here. We therefore set $u_0 = 0.001$ as a minimum value. Therefore, this condition gives an array between

$$0.001 \leq u_0 \leq 1.0. \tag{3.4}$$

For a given event, this parameter is chosen by a uniform random distribution.

- Time of peak magnification t_0

Since microlensing events can occur at any time, t_0 is randomly distributed in time. We confine the range of t_0 to between 0 and 30 days due to the restriction on Euclid's pointing (see Section 2.4.3). Hence, we have

$$0 \leq t_0 \leq 30.0. \tag{3.5}$$

- The Einstein radius crossing time t_E

The distribution of t_E is observed to be a log-normal distribution. The probability of event time scale t_E is therefore

$$P(\ln t_E) \propto \exp\left[-\frac{(\ln t_E - \mu)^2}{2\sigma^2(\ln t_E)}\right], \tag{3.6}$$

where μ is the mean value of $\ln t_E$, σ is its standard deviation. From a fit to the efficiency-corrected timescale histogram in Figure 13 of (Wyrzykowski et al., 2014), we take $\ln(t_E/\text{days}) = \mu = 2.5$ and $\sigma = 1$. Values of t_E are generated randomly from this distribution. An example of microlensing light curve with these parameters can be described as Figure 3.1.

3.3 Generating transit signals

To model the transit signal from a microlensed source star, we need to consider the properties of the host star and its planet. For simplicity, we ignore the effect of

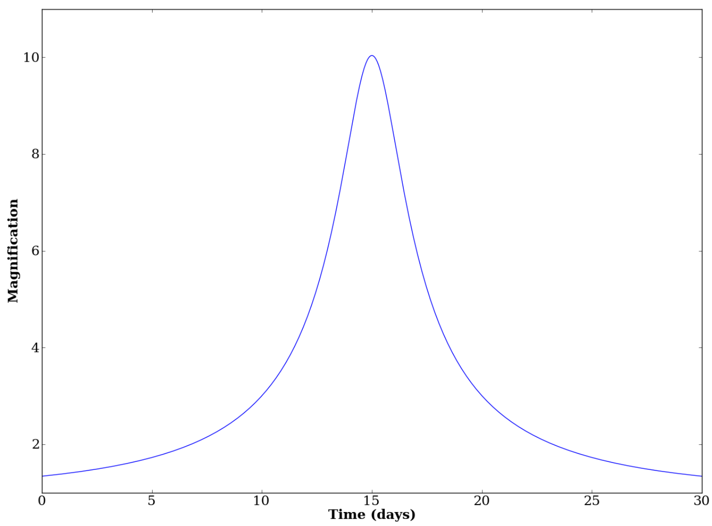

Figure 3.1: A theoretical microlensinig light curve. In this example, we set specific $t_0 = 15.0$ days, $t_E = 15.0$ days and $u_0 = 0.1$.

limb darkening of the source and we assume circular planetary orbits. We also do not model the secondary transit signal. For the generation of transit light curves, we use Equations 1 of Mandel & Agol (2002) to describe the fraction F of the star light which is dimmed due to the transit. These equations are expressed as

$$F(p, z) = 1 - \lambda(p, z), \tag{3.7}$$

where $p = r_p/r_*$ is the radius size ratio between the planet and star, z is the projected distance of the planet from the centre of the star in units of star size. The parameter λ is expressed as

$$\lambda(p, z) = \begin{cases} 0 & 1 + p < z, \\ \frac{1}{\pi}\left[p^2\kappa_0 + \kappa_1 - \sqrt{\frac{4z^2-(1+z^2-p^2)^2}{4}}\right] & |1-p| < z \leq 1 + p, \\ p^2 & z \leq 1 - p, \\ 1 & z \leq p - 1, \end{cases} \tag{3.8}$$

where $\kappa_0 = cos^{-1}[(p^2+z^2-1)/2pz]$ and $\kappa_1 = cos^{-1}[(1-p^2+z^2)/2z]$ which contribute to the transit depth slopes.

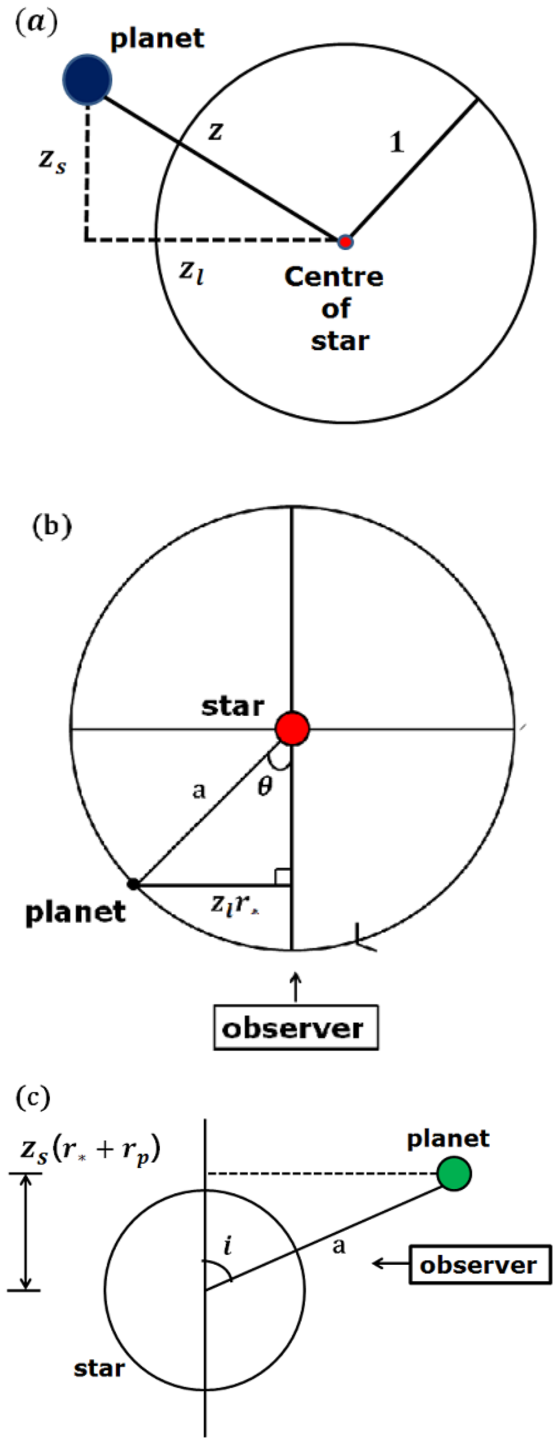

Figure 3.2: The transit geometry. (a) The relation between the horizontal and vertical components of the projected host separation z. All sizes are normalized by r_*. (b) The projected distance $z_l r_*$ between the host star and planet. a is the physical host separation. (c) The relationship between a physical host separation a and the vertical component of projected host separation $z_s r_*$. i is the orbital inclination.

z comprises a horizontal component z_l and vertical component z_s. From Figure 3.2, the horizontal component of projected host separation z_l can be derived as

$$z_l = \frac{a}{r_*}\cos(\frac{2\pi t}{P} + \theta) \tag{3.9}$$

with a being the planet-host separation, t is time, P is the orbital period and θ is the phase angle. In order to consider the vertical component of z, we need an inclination of the planet's orbit. In Figure 3.2, if i is smaller than some minimum value, there is no transit event. Therefore, the range of inclination is between $i_{\min}$ and the line-of-sight inclination $\pi/2$. Since our aim is to check if there is a transit, the symmetric phase between $\pi/2$ to π does not need to be considered. $i_{\min}$ is given as

$$i_{\min} = cos^{-1}(z_s(r_* + r_p)/a), \tag{3.10}$$

hence, z_s can be generalized as

$$z_s = \frac{a}{r_*}cosi. \tag{3.11}$$

Therefore, the two-dimensional z (see Figure 3.2) can be expressed as

$$z = \sqrt{z_l^2 + z_s^2}. \tag{3.12}$$

3.3.1 Generating parameters and conditions

As the value of λ is a function of p and z, both depend on planet and host parameters. We therefore discuss how these values are generated.

3.3.2 Host star parameters

For the host star properties, we used the data from the Besançon Galactic model. A synthetic star catalogue was generated for direction towards the Galactic Bulge at Baade's Window, close to the centre of the proposed ExELS fields

($l = 1.1°$,$b = -1.7°$). For each star, the catalogue provides: the stellar H-band apparent magnitude; the mass (M_*); the radius (r_*); and the distance from the observer. For each source, we also had a microlensing statistical weight which is discussed further in Section 4.4.1.

Planet parameters

For the planet radius, we select uniformly within the interval:

$$0.009 \leq r_p/R_\odot \leq 0.15, \tag{3.13}$$

which for a solar-type star corresponds to Earth to Jupiter sized planets.

Parameter θ gives an initial random location on its trajectory. It is determined from 0 to 360 in units of degree which is equivalent to 0 to 2π

$$0° \leq \theta \leq 360°. \tag{3.14}$$

The physical host separation a is determined from minimum and maximum allowed values. When it comes to the minimum orbital radius, we set

$$a_{min} = 3r_\star. \tag{3.15}$$

We made the maximum host separation correspond to a 10-day orbital period. The reason for this is so that ExELS can observe a minimum of 3 transits within a 30-day observing window. The maximum host separation is derived from Kepler's 3rd law

$$P^2 = \frac{4\pi^2 a^3}{GM_*}, \tag{3.16}$$

where G is the gravitational constant. As a result of this, the detectable host separation of all candidates in the Galactic model lies in the range:

$$3\frac{r_*}{R_\odot} \leq \frac{a}{R_\odot} \leq 0.09 \left(\frac{M_*}{M_\odot}\right)^{1/3} \left(\frac{AU}{R_\odot}\right). \tag{3.17}$$

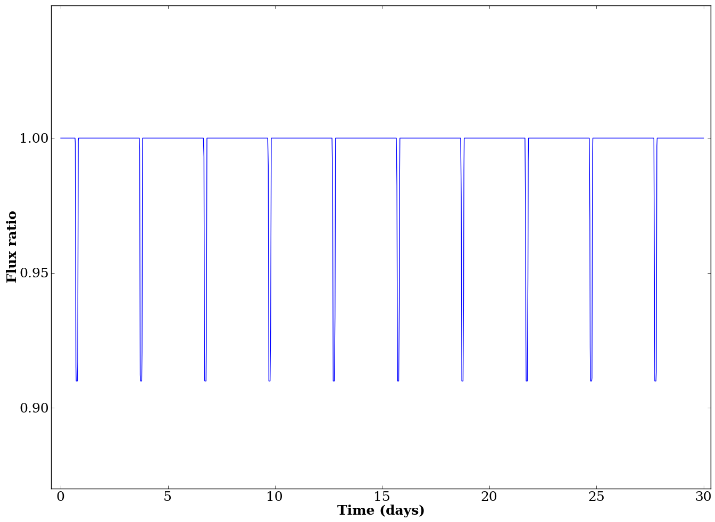

Figure 3.3: An illustration of a theoretical transit light curve. Periodic transit dips can be seen from the light curve every 3 days. Secondary transit and limb darkening effects are ignored.

For the simulation, a was selected from a logarithmic distribution within these bounds. After selecting a for a given system, we can compute the planet period using Equation 3.16. The observable signal itself has a duration given by the duration of transit of the planet across the host star ΔT. We adopted the equation (14) from Winn (2010):

$$\Delta T = \frac{P}{\pi} sin^{-1} \left[\frac{r_*}{a} \frac{\sqrt{(1+p)^2 - z_s^2}}{\sin i} \right]. \tag{3.18}$$

By defining those paramters, we can generate relative flux transit light curves such as the example shown in Figure 3.3.

3.4 Generating realistic light curves with Euclid photometry

In order to generate realistic scenarios, we need to consider Euclid's performance and also observing conditions. We used the NISP camera's H-band filter as proposed by Penny et al. (2013) for ExELS. Relevant NISP detector parameters are listed in Table 3.1.

In this simulation, we set the PSF size of 0.45 arcsecond as the aperture for flux

Table 3.1: The properties of the Euclid NISP instrument in the H-band (Penny et al., 2013).

Quantity	Variable	Values
PSF FWHM (arcsec)	$\phi/2$	0.45
Zero-point (ABmag)	M_{zp}	24.92
Diffuse background (ABmag arcsec^{-2})	M_{BG}	21.4
Exposure time (secs)	t_{exp}	54

measurements. From Table 3.1, we take a H-band background surface brightness of 21.4 mag/arcsec^2. The background magnitude (M_{AP}) within a PSF aperture of size ϕ can be calculated as

$$M_{AP} = M_{BG} - 2.5log_{10}(\frac{\pi\phi^2}{4}), \tag{3.19}$$

where M_{BG} is a background surface brightness and $M_{AP} = 21.89$ using the values from Table 3.1.

We are now able to generate theoretical light curves using Euclid's photometry sensitivity. In order to make the simulation more efficient, we make a cut on signal-to-noise ratio to select light curves with potentially detectable transit signals.

3.4.1 Selection by signal-to-noise ratio

Since photon counting follows the Poisson distribution, the photon noise is given by the square root of the signal. In observation, however, the collected signal includes both the target and background signals. Therefore, both noise contributions should be included in the photon noise. For that reason, signal-to-noise ratio (SNR) is expressed as

$$\text{SNR} = \frac{(n_{ps} \times t_{\text{exp}} \times A)}{(\sqrt{(n_{bg} \times t_{\text{exp}}) + (n_{ps} \times t_{\text{exp}} \times A)}}, \tag{3.20}$$

where A is the maximum magnification by microlensing effect and t_{exp} is the exposure time for H-band of the NISP camera (Table 3.1). The reason for multiplying by A is to estimate the maximum detectability of transit signals from a source star which may originally be too faint to detect. n_{bg} is the number of background photons per second within an aperture of ϕ. Therefore, with Mag_{AP}, n_{bg} can be estimated as

$$n_{bg} = 10^{-0.4(M_{AP}-M_{zp})} = 16.3 \text{ photons sec}^{-1}. \tag{3.21}$$

Here, M_{zp} is the zero-point magnitude of H-band (Table 3.1). In the same manner, the number of photons per second from the source star n_{ps} can be calculated as

$$n_{ps} = 10^{-0.4(H_{*}-M_{zp})}. \tag{3.22}$$

Here, H_* is the H-band magnitude of the Besançon catalogue star. Hence, n_{ps} varies with each star.

Since u_0 determines the peak magnification, we randomly generate a value between 0.001 to 1 for each star (see Section 3.2.1). We then apply Equation 3.20 and demand $SNR \geq 50$. Sources which fail this cut are discarded and we proceed to generate light curves for which are passed.

3.5 Realistic photometry from the combined transiting and microlensing light curves

In terms of flux, the signal from a microlensed transiting system is

$$F = F_{\mathrm{ml}} \times f_{\mathrm{tr}} = f_{\mathrm{tr}} A F_{*}, \tag{3.23}$$

where $F_{\mathrm{ml}} = AF_*$ is the flux due to microlensing, with A the magnification factor, and f_{tr} is the relative flux fraction due to the transit. Figure 3.4 is a theoretical example of a combined light curve. To transform Equation 3.23 onto a magnitude scale, we convert as follows:

$$M = H_{*} - 2.5log_{10}(f_{\mathrm{tr}} A). \tag{3.24}$$

where H_* is the H-band magnitude of source star corresponding to F_*.

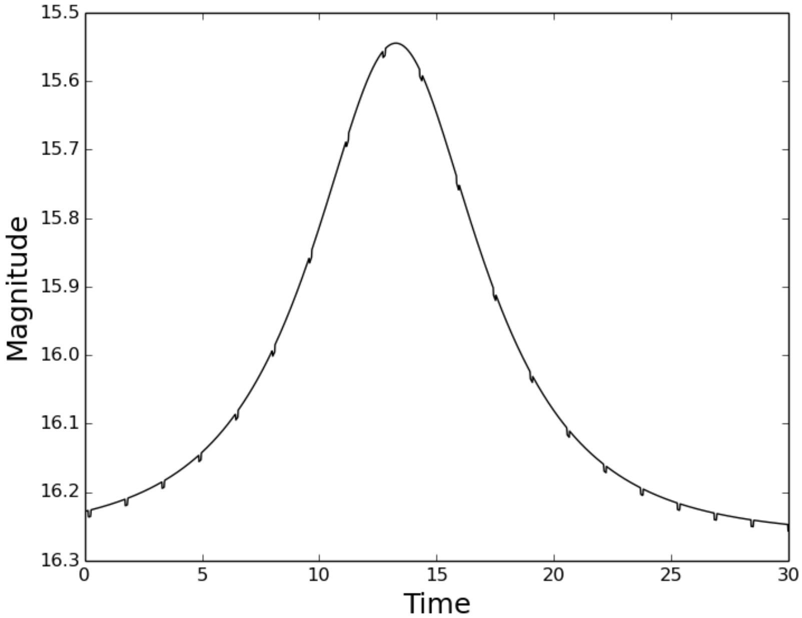

Figure 3.4: An example of a combined light curve with microlensing and transit effects on a magnitude scale. The transit dips are proportional to value of p^2 in Equation 2.3.

3.5.1 Generating uncertainties

Real data contain uncertainties which come from for example, background signals or the instrument itself. In this simulation, we consider only photon noise. The number of detected photons is given by

$$N = t_{exp} 10^{-0.4(M-M_{zp})}. \tag{3.25}$$

The photon noise is therefore $\delta N = \sqrt{N}$. The corresponding magnitude uncertainty is

$$\delta M = \left| \frac{\partial M}{\partial N} \right| \delta N = \frac{2.5}{\ln 10} \frac{\delta N}{N} = \frac{2.5}{\ln 10} \frac{1}{\sqrt{N}}. \tag{3.26}$$

As a next step, we generate a random realization M_r for the magnitude given an expected value M and its uncertainty δM. We generate M_r by assuming that it is Gaussian distributed about M with a dispersion given by δM. The probability distribution p for M_r is therefore:

$$p(M_r) = \frac{1}{\sqrt{2\pi(\delta M)^2}} e^{-\frac{(M_r - M)^2}{2(\delta M)^2}}. \tag{3.27}$$

Figure 3.5 and 3.6 are theoretical and realized version including photon noise of the same light curve.

ExELS can continuously observe for a period of 1 month with 20 minutes cadence (Penny et al., 2013). This implies n=2160 epochs over a span of one month.

3.6 Fitting for microlensing

As we will not know the exact value of each parameter for a real observation due to noise and finite sampling, we fit our simulated events to determine what information we can extract. We fit a microlensing model to our simulated data to see if there are transit signals detected as residuals. We use a standard χ^2 goodness-of-fit statistic

$$\chi^2 = \sum_{i=1}^{n} \left(\frac{M_{r,i} - M_{ml,i}}{\delta M_i} \right)^2, \tag{3.28}$$

where n is the total number of data points and $M_{ml,i}$ is the microlensing model prediction at epoch i and $M_{r,i}$ is the simulated observation.

For the fitting, initial guesses on the microlensing parameters are needed. We need to consider four parameters (H_*, u_0, t_0 and t_E). As an initial H_* value, we used a median value of $M_{r,i}$. Since u_0 defines the magnification, the parameter can be inferred from the maximum and minimum magnitudes ($M_{\max}, M_{\min}$) in the simulated light curve. Therefore, a guessed u_0 can be set as

$$u_{0,\text{guess}} = 10^{-0.4(M_{\min} - M_{\max})}. \tag{3.29}$$

We adopt $t_{0,\text{guess}}$ as the epoch where $M_{r,i} = M_{\min}$. Finally, we adopt mean value of $\ln t_E = \mu = 2.5$ as defined in Equation 3.6.

Using the initiall guesses we performed the fit with the `scipy.optimize.leastsq`

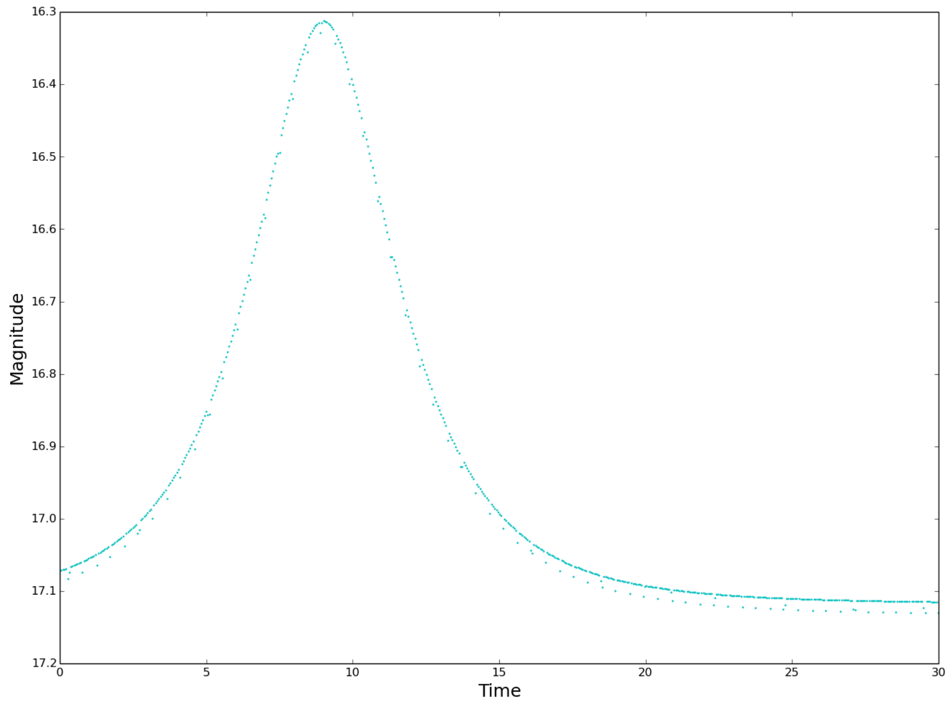

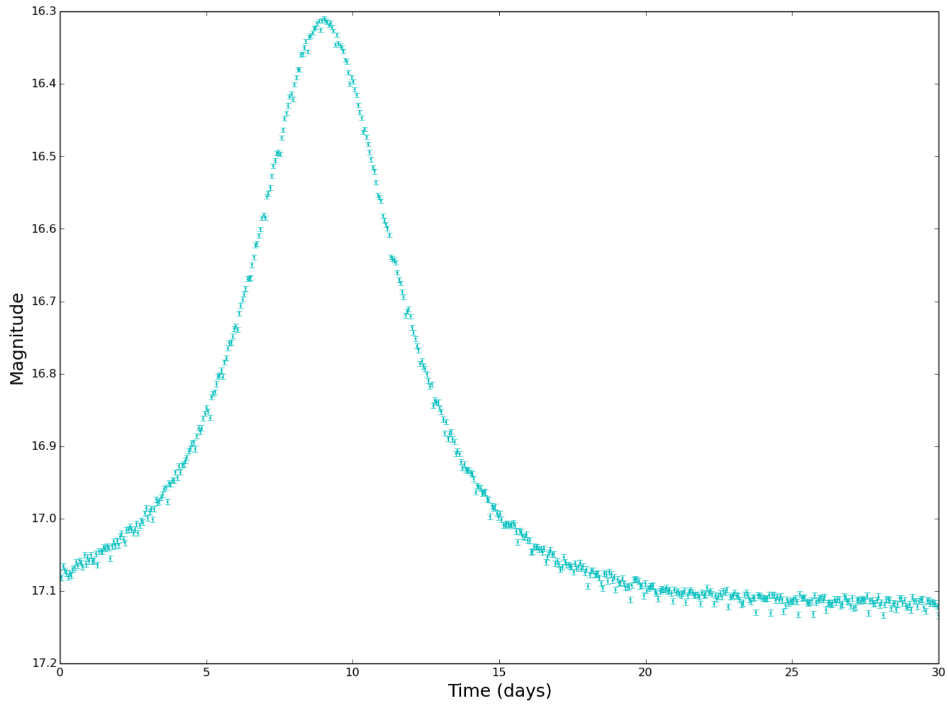

Figure 3.5: An example of a transiting+microlensing light curve (Top) along with an uncertainty (Bottom) assuming Euclid's photometric sensitivity. Both graphs are generated with same parameters $P = 0.48$ days, $u_0 = 0.52$, $t_0 = 9.0$ days, $t_E = 38.64$ days and $p = 0.12$. The actual observation cadence is four times greater than shown here.

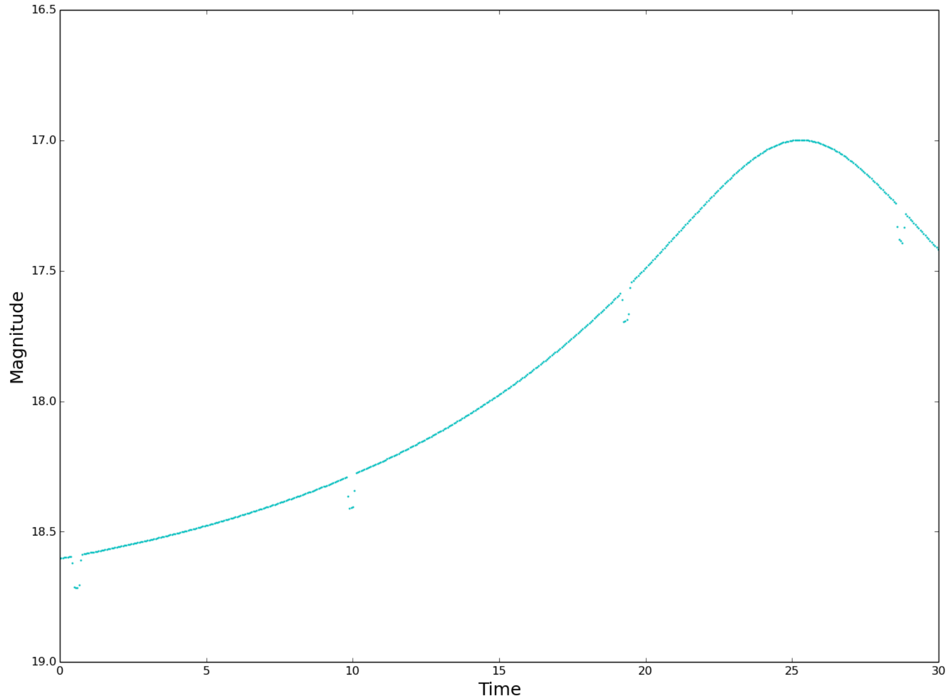

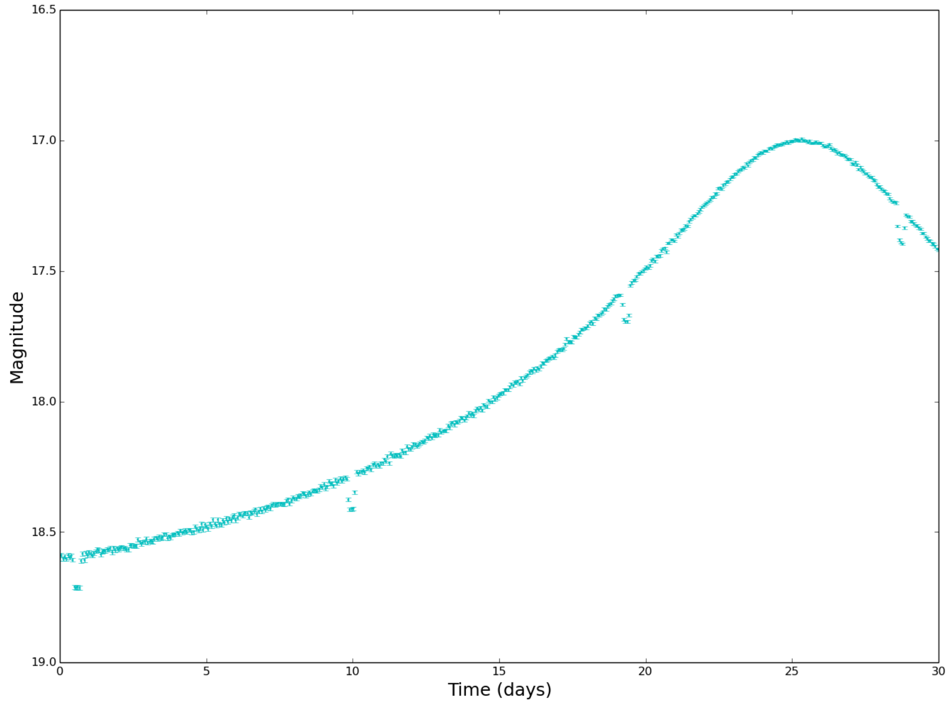

Figure 3.6: Another example of a transiting+microlensing light curve (Top) along with an uncertainty (Bottom) assuming Euclid's photometric sensitivity. Both graphs are generated with same parameters $P = 9.38$ days, $u_0 = 0.18$, $t_0 = 25.3$ days, $t_E = 23.63$ days and $p = 0.33$. The actual observation cadence is four times greater than shown here.

routine from the Python SciPy[1] package.

3.6.1 Extracting transit signals from the simulated data

As can be seen from Equation 3.20, the effect of microlensing magnification is to improve the transit signal's SNR. However, in order to extract transit signals, we need to divide the simulated flux data points by the microlensing fit or, equivalently, subtract the microlensing fit from the data when both are expressed as magnitudes. The residual transit light curve ($M_{\rm tran}$) can therefore be expressed simply as

$$M_{\rm tran} = M_r - M_{ml,fit}, \tag{3.30}$$

where M_r and $M_{ml,fit}$ are the data and microlensing model with fitted parameters, respectively (defined by Equation 3.27). Figure 3.7 and 3.8 show sum extracted transit signals from the simulation to increase signal-to-noise ratio.

3.7 Estimating trial period from the scenarios

In order to fit the transit signals, we used `kepbls` module[2] from the Python software package `pyke`[3] based on a method developed by Still & Barclay (2012). This code is based on a Box Least Square (BLS) fitting method (Kovács et al., 2002). The BLS method is tailor-made for fitting box-shape profiles which is good first order description of a transit light curve. The main advantage of the BLS method is that is computationally highly efficient in such case. However, possible inefficiencies may occur when transit light curves depart strongly from a box profile, e.g. when limb darkening effects are very strong or in the presence of star spots.

3.7.1 Setting conditions for estimating trial periods

We applied the BLS method in two stages. The first stage provided approximate

[1]http://docs.scipy.org/doc/scipy-0.14.0/reference/generated/scipy.optimize.leastsq.html
[2]http://keplerscience.arc.nasa.gov/PyKE.shtml
[3]http://pyke.sourceforge.net/index.html

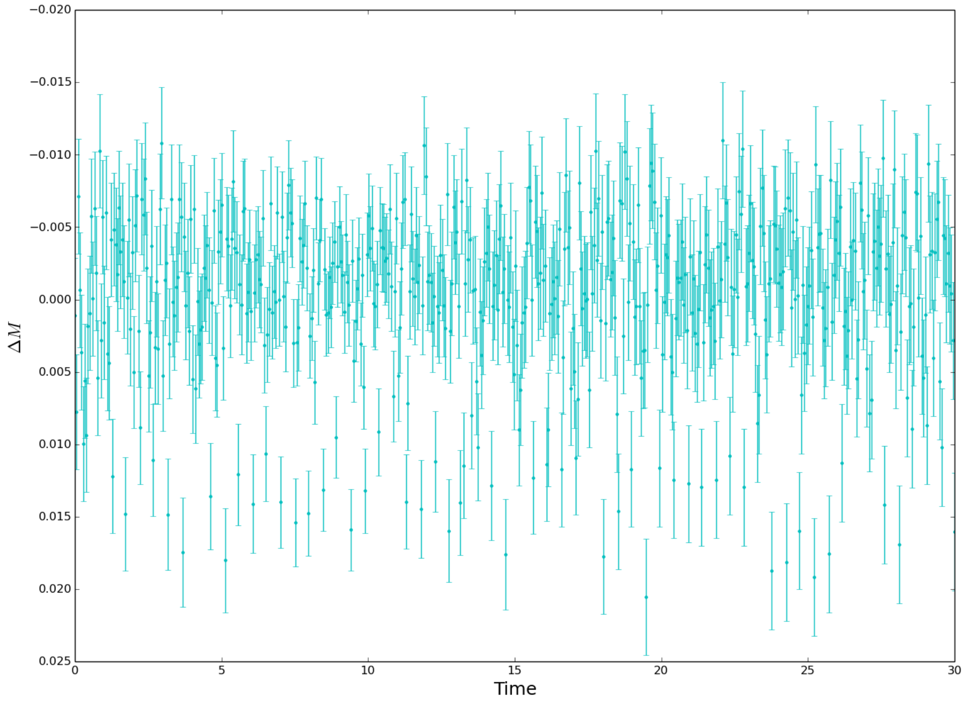

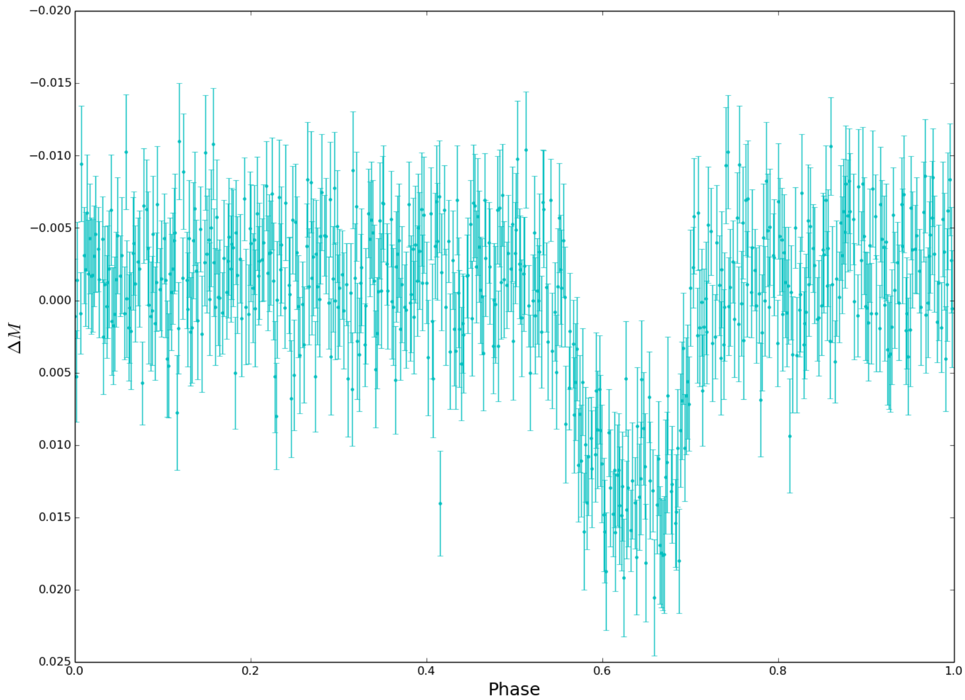

Figure 3.7: Examples of an extracted transit signals (Top) and its folded version normalized by Period (Bottom) from Figure 3.5.

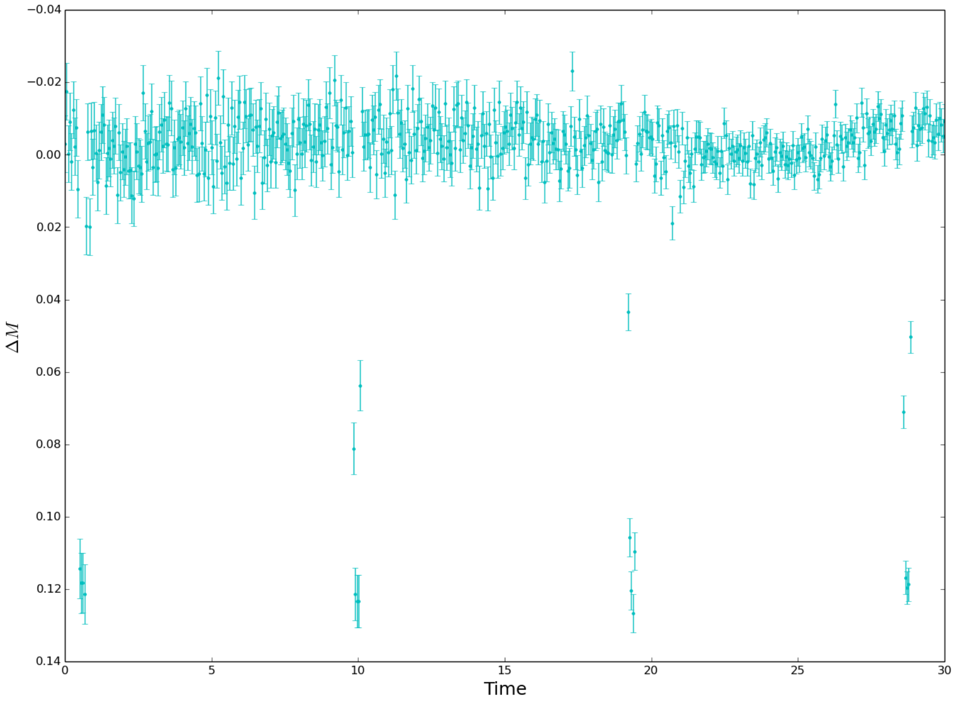

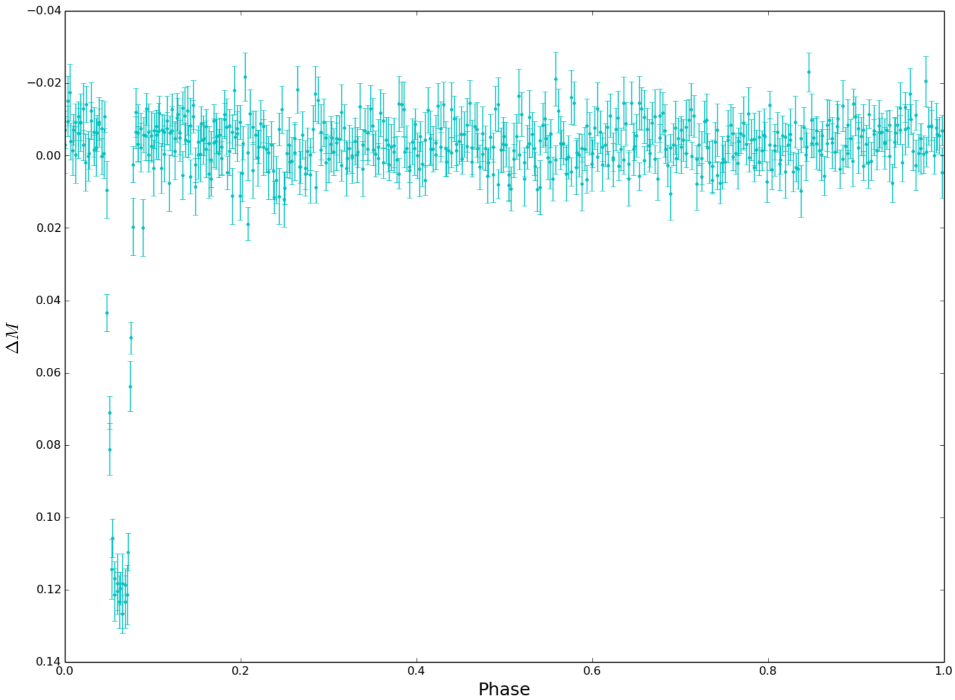

Figure 3.8: Examples of an extracted transit signals (Top) and its folded version normalized by Period (Bottom) from Figure 3.6.

set of parameters and in the second stage we performed a higher resolution run around the initial solution.

In the `kepbls` module, there are six variables to input. These are: `minper`; `maxper`; `mindur`; `maxdur`; `nsearch`; and `nbin`. These are now briefly described and their values for the first stage run are given.

- `minper`, `maxper`

These parameters, in units of days, set the minimum and maximum search period. Since we wish to avoid solutions which are harmonics of the true period ($P_{\rm true}$), we restricted `minper` and `maxper` to $0.55\,P_{\rm true}$ and $1.95\,P_{\rm true}$, respectively. Additionally, we found that `kepbls` was unable to search period below 0.25 days for our assumed cadence and therefore, we rejected sets of parameters which had $0.55 \times$ period ≤ 0.25 days. We did not count these cases as failed detections.

- `mindur`,`maxdur`

These parameters refer the minimum and maximum transit duration within the parameter search. These are set to values of 1 and 12 hours as a crude search and 1.2 and 11 hours for the higher resolution search, respectively, corresponding to the smallest and largest transit durations across all our simulated transit systems.

- `nsearch`,`nbin`

The parameter `nsearch` determines the number of trial periods to search between `minper` and `maxper` for a given data set. We set `nsearch`$= 100$ for both the initial and final run. The `kepbls` module works by folding the original time series by a trial period and then binning the folded time series before BLS fitting. `nbin` sets the number of bins for the folded light curve and we set it to a value of `nbin`$= 100$ for the initial run.

We inspect the relative accuracy of the period solution from the first run to determine if a second higher resolution run is necessary. The maximum relative precision of the first run is given by the period span ($1.95\,P_{\rm true} - 0.55\,P_{\rm true} = 1.4\,P_{\rm true}$)

and the number of search bins (`nsearch`= 100) and is therefore $0.014\,P_{\rm true}$, giving a relative period precision of 0.014. If the period solution from the first run is more than 1.4% away from the true (simulated) value, then the transit is deemed to be undetected. If it lies within 1.4% of the true value, a second higher resolution fit is performed over a period interval of $(0.97\,P_{\rm true}, 1.03\,P_{\rm true})$, with `nbin`= 30. If after the second run the fitted period is within 1% of the simulated value, we deemed the transit as detected. Figure 3.9 shows the histogram of the precision of fitted periods for all simulated events with respect to their true (simulated) period. There are 7339 candidates which were detected from among 9311 initial candidates. From Fig 3.9, we see that around 3,800 candidates have their period determined to within 1.4%, with the remainder having poor period determination with a roughly uniform distribution of relative period precision. This tail of poorly characterised transit is caused by low SNR transit signal. Whilst the underlying microlensing event is detected with SNR $\geq$ 50, the transit signals represent deviations which are often less than 1% of the signal. When the transit signal is comparable to the level of the noise, the BLS routine will typically fail to find a reliable period. We discuss the detected fraction in more detail in Section 4.4.

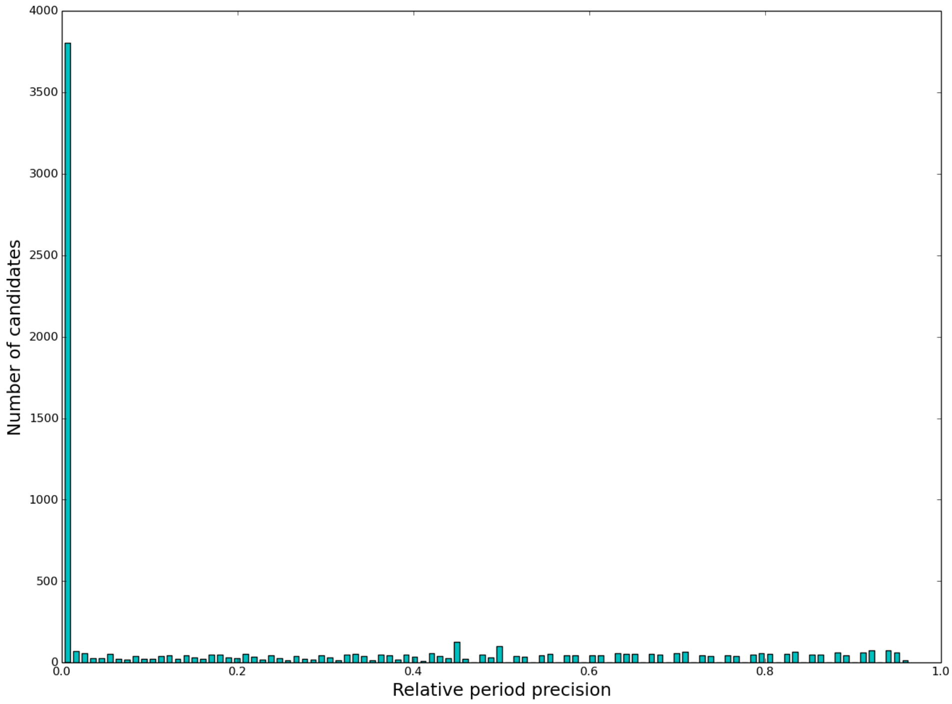

Figure 3.9: The histogram of the period precision after the first fitting run. As can be seen from the histogram, a significant number of candidates have period determinations within 1.4% of the true value. These cases have a more accurate fit determined by a second run. Those with fitted periods more than 1.4% away from the true value were rejected.

Chapter 4

Analysis of the simulation results

4.1 Recovery of microlensing parameters

In this section, we dicuss the correspondence between true and fitted microlensing parameters: baseline H-band magnitude; u_0; t_0; and t_E.

4.1.1 Recovery of the H-band magnitude

The recovery of the baseline H-band magnitude in general is very good as can be seen from Figure 4.1. However, there is a clear tendency of increased scatter between magnitude around 18 and 22. 94% of the fitted magnitudes are within 0.1 mag of the true H-band magnitude. In addition, approximately 20% (1502) of candidates are outside of 3σ statistically. The possible reasons for the more scattered values may come from the low magnification of relatively faint sources or from light curves involving a large planet-star radius ratio and short transit period which can bias the baseline magnitude estimation. Figure 4.1 indicates that the main reason is from faint sources.

4.1.2 Recovery of u_0

In the same manner of H-band magnitude, u_0 is also a factor which affects the observed magnitude. Hence, low magnification (large u_0) or high planet-star radius ratio coupled with a short transit period can cause poor fitting results. As can be

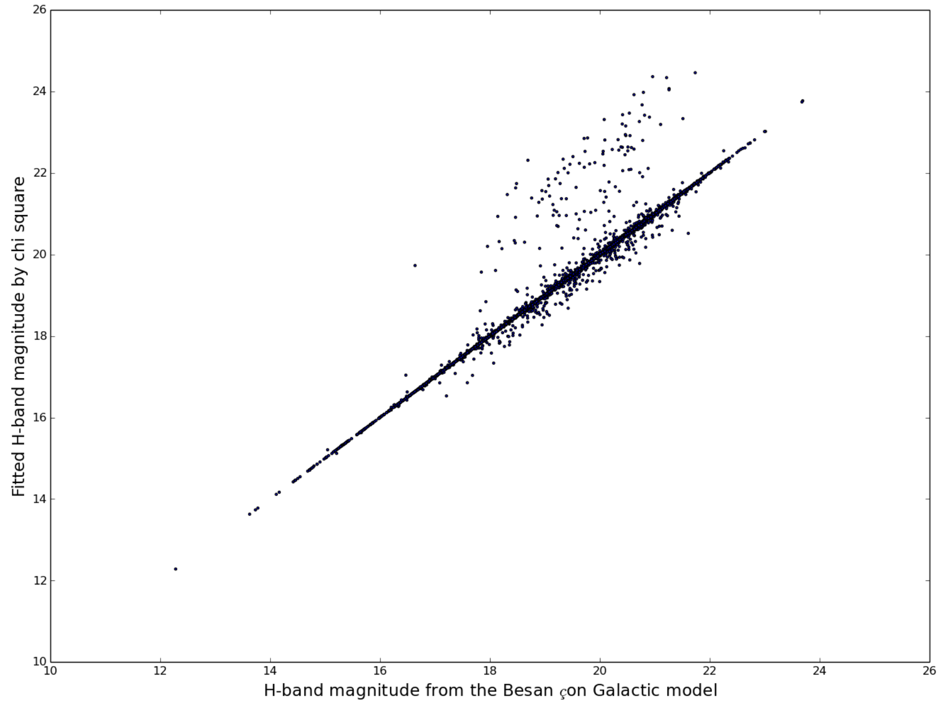

Figure 4.1: The correspondence between the true baseline H-band magnitude and the fitted value for our simulated light curves.

seen from Figure 4.2, generally the recovered u_0 corresponds very well with the true u_0, with 93% of fitted values being within 10% of the true value. However, for large impact parameters there is a clear tendency for the scatter to increase, with the number of poorly determined values increasing dramatically from around $u_0 \sim 0.3$. Furthermore, the value gaps between randomly generated u_0 and fitted u_0 are larger above the main correlation stream.

4.1.3 Recovery of t_0

As can be seen from Figure 4.3, it can be seen that the fitted value of t_0 appears generally to be very reasonable. It is noticeable that there is an increased scatters towards the lowest and highest values. For these values essentially only half of the light curve lies within the ExELS's observing window. However, 99% of simulated events have a fitted t_0 within 10% of the true value.

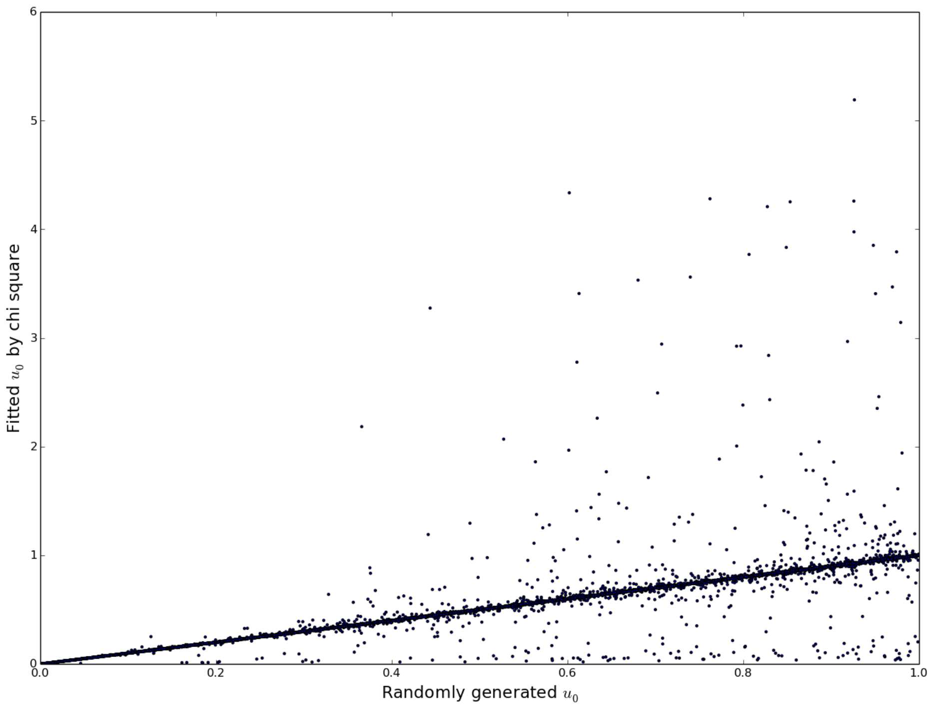

Figure 4.2: The correspondence between true and fitted values for u_0.

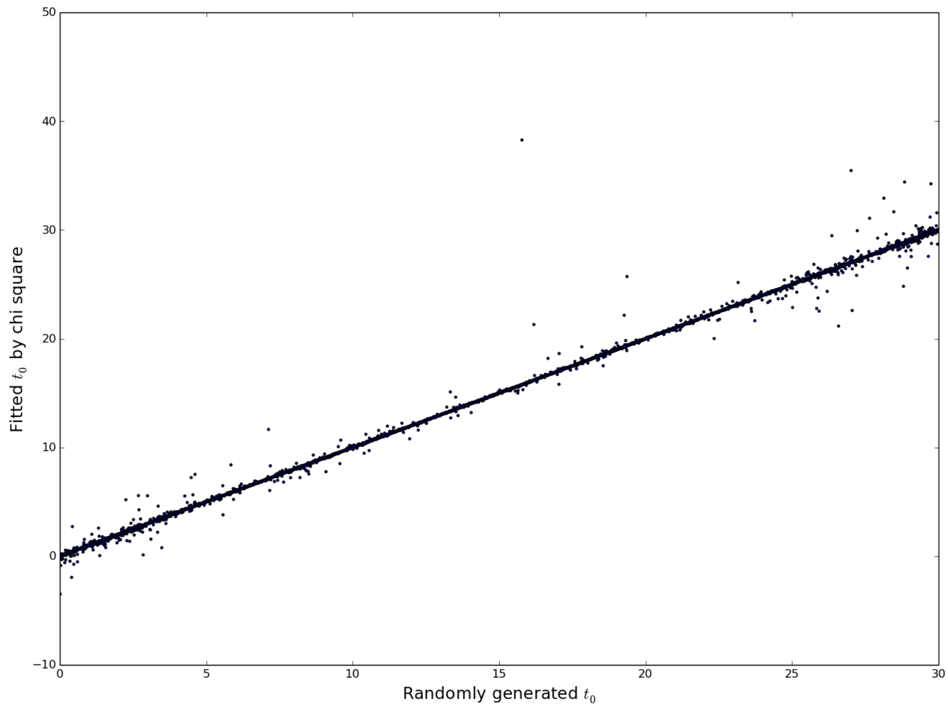

Figure 4.3: The correlation between true parameters of t_0 and fitted parameters of t_0.

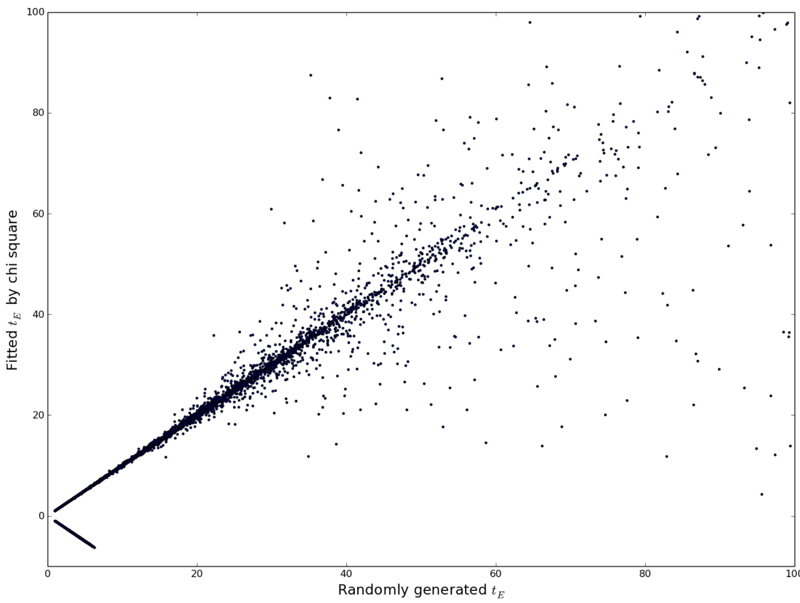

Figure 4.4: The correlation between true parameters of t_E and fitted parameters of t_E.

4.1.4 Recovery of t_E

As can be seen from Figure 4.4, generally t_E is well fitted. However, poor fitting results are evident for $t_E \gtrsim 20$ days and there are also some negative t_E results for small event durations. When it comes to the poor fitting results after roughly 20 days, this is expected because of the finite ExELS's continuous observation window of 30 days. Since there is no information after 30 days when fitting, poor fitting results may occur more frequently when t_E is large. As for the negative t_E values, the fit χ^2 is sensitive to t_E^2, rather than t_E, through Equation 2.11 and therefore the negative values simply reflect this degeneracy.

4.2 Examples of non-selected light curves

4.2.1 Light curves which fail the signal-to-noise ratio cut

Because we set the signal-to-noise ratio cut at SNR > 50 at the maximum magnificantion, u_0 and the source photon count n_{ps} play an important role in determining the SNR by Equation 3.20. Therefore, low SNR implies we have small n_{ps} or low magnification or both. To illustrate the quality of the failed events, we plot three types of light cuvres with different SNR from 35 to 50, close to the border line of our cut. As can be seen from Figure 4.5, 4.6 and 4.7, lower SNR light curves typically have larger u_0 values. For clarity, the plotted observation epochs are reduced by six times compared to the actual ExELS's proposed cadence of 2160 points over 30 days. Despite transit depths in excess of 1% (equivalent to Jupiter transiting the Sun), there are no obvious transit signals to be seen in Figure 4.5 or 4.6. While the transit signals are visible in Figure 4.7, this is only because of an extreme transit depth of 9%. Our chosen SNR threshold of 50 is reasonable.

4.2.2 Examples of light curve which fail the period precision cut

The period precision plays an important role in our simulation as a detectable exoplanet determining factor. Figure 4.8, 4.9 and 4.10 are examples of light curve residuals which fail the period precision cut of 1% (see Section 3.7.1). As discussed in Section 3.7.1, if the level of SNR of the transit residual signal is comparable to the noise, the BLS routine will typically fail to accurately characterize the period even though the underlying microlensing signal component will have SNR ≥ 50 (see Figure 4.8 and 4.9). Figure 4.10 shows a clear transit signal which could have been classified as a detectable candidate but, it just fails due to our the period precision cut. For clarity, the actual observation cadance is two times greater than shown here.

4.3 Examples of selected light curves

4.3.1 The effect of magnification on the transit light curve quality (t_E)

Since the main goal of this work is to detect transit signals from a microlensed

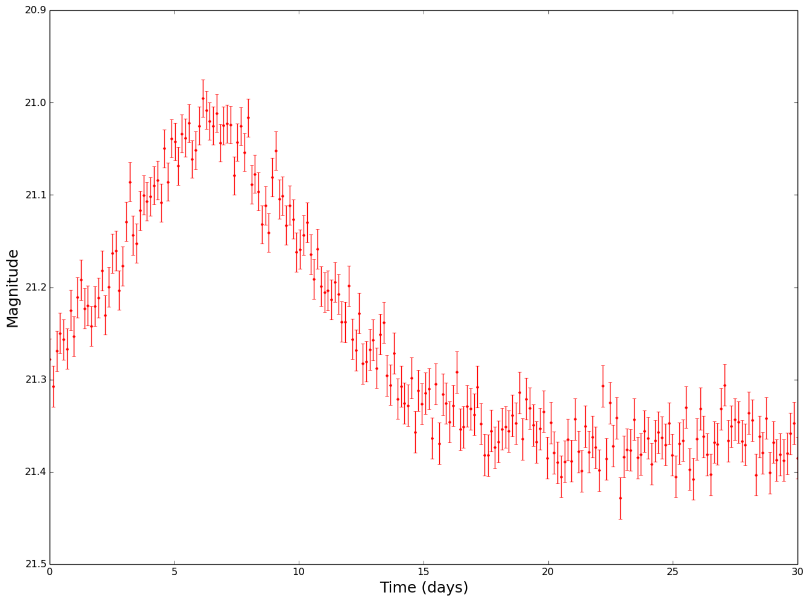

Figure 4.5: An example of a microlensed transiting exoplanet signals with fails our SNR threshold of 50. This event has SNR= 37, a transit period of 9.7 days, an impact parameter $u_0 = 0.94$, time of maximum magnification $t_0 = 6.4$ days, Einstein radius crossing time $t_E = 4.4$ days and star-planet radius ratio $p = 0.13$. Note that the proposed ExELS survey will have an observing cadence six times greater than shown here.

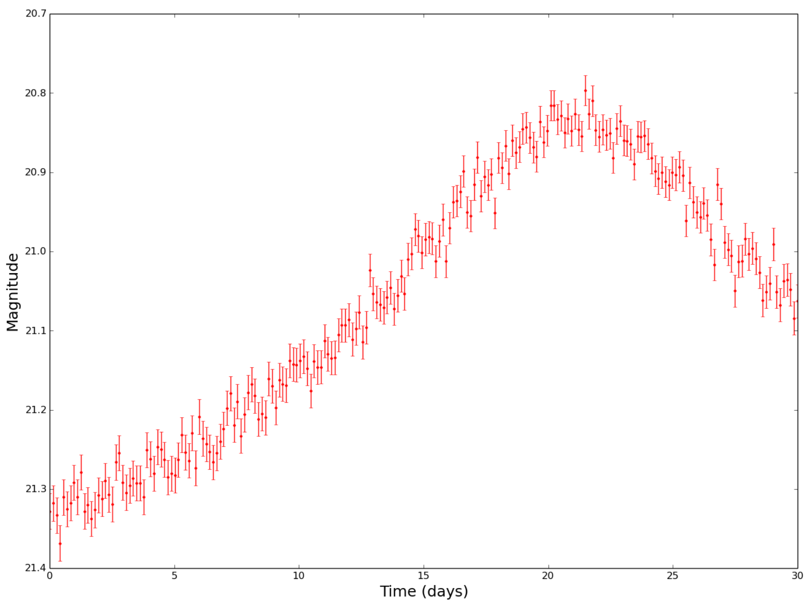

Figure 4.6: An example of a microlensed transiting exoplanet signals with fails our SNR threshold of 50. This event has SNR= 41, a transit period of 8.7 days, an impact parameter $u_0 = 0.7$, time of maximum magnification $t_0 = 21.3$ days, Einstein radius crossing time $t_E = 12.25$ days and star-planet radius ratio $p = 0.12$. Note that the proposed ExELS survey will have an observing cadence six times greater than shown here.

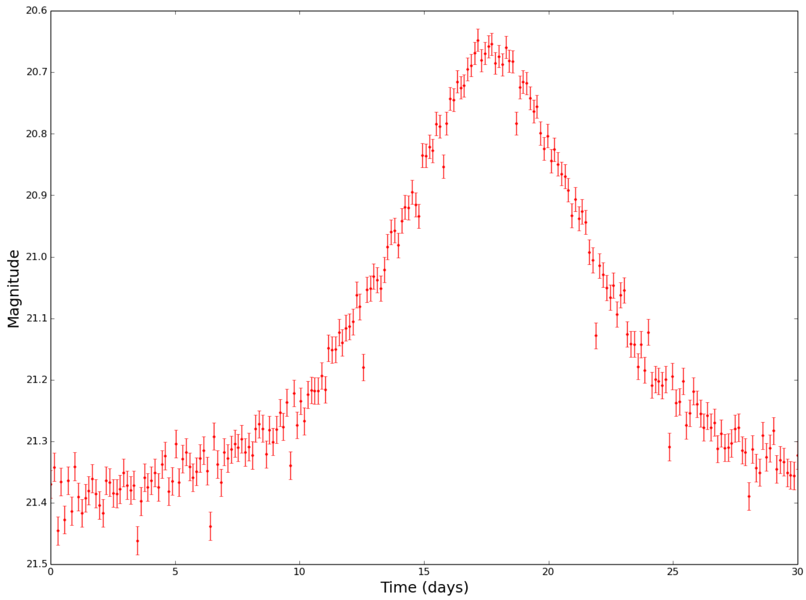

Figure 4.7: An example of a microlensed transiting exoplanet signals with fails our SNR threshold of 50. This event has SNR= 45.4, a transit period of 6.1 days, an impact parameter $u_0 = 0.56$, time of maximum magnification $t_0 = 17.71$ days, Einstein radius crossing time $t_E = 6.27$ days and $p = 0.3$. Note that the proposed ExELS survey will have an observing cadence six times greater than shown here.

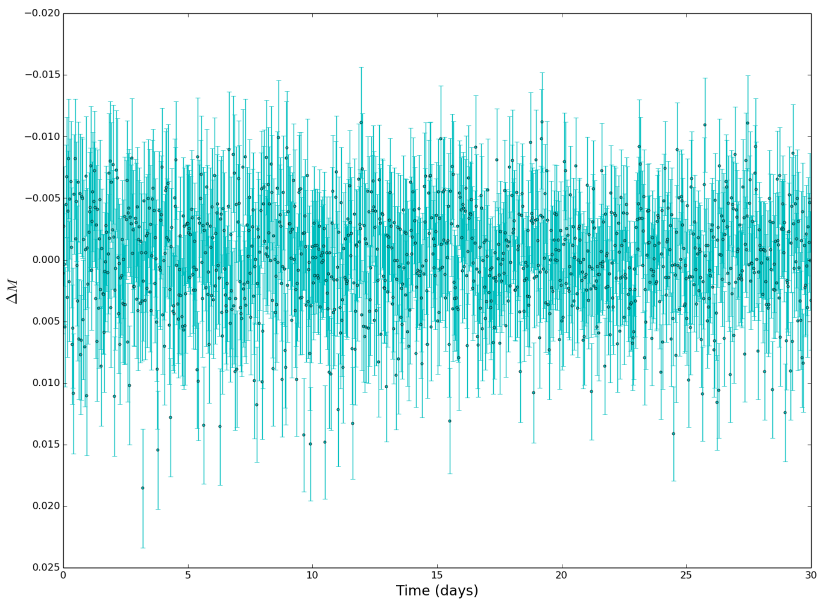

Figure 4.8: A residual transit light curve (with the microlensing fit subtracted off) with a period precision of 94% between the fitted and true period. The true period is 1.1 days and the star-planet radius ratio is $p = 0.09$.

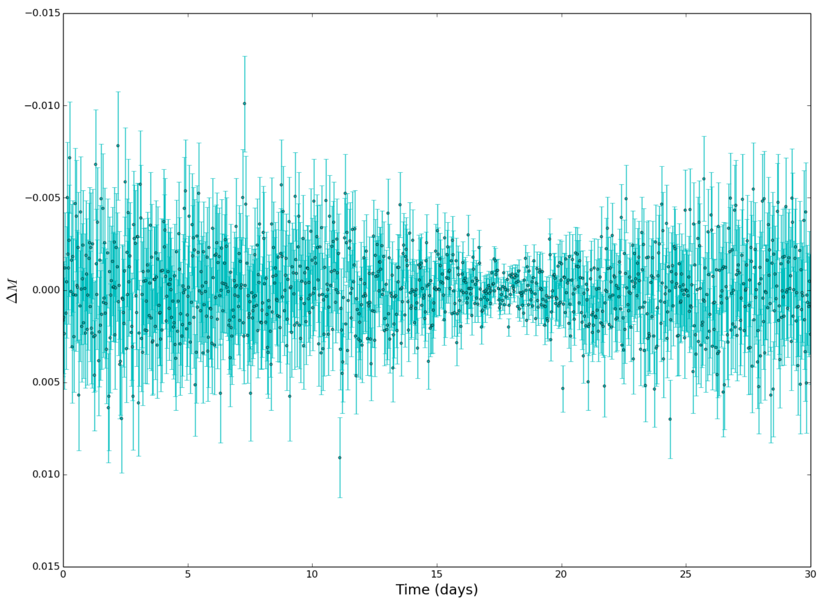

Figure 4.9: A residual transit light curve (with the microlensing fit subtracted off) with a period precision of 52% between the fitted and true period. The true period is 1.1 days and the star-planet radius ratio is $p = 0.05$.

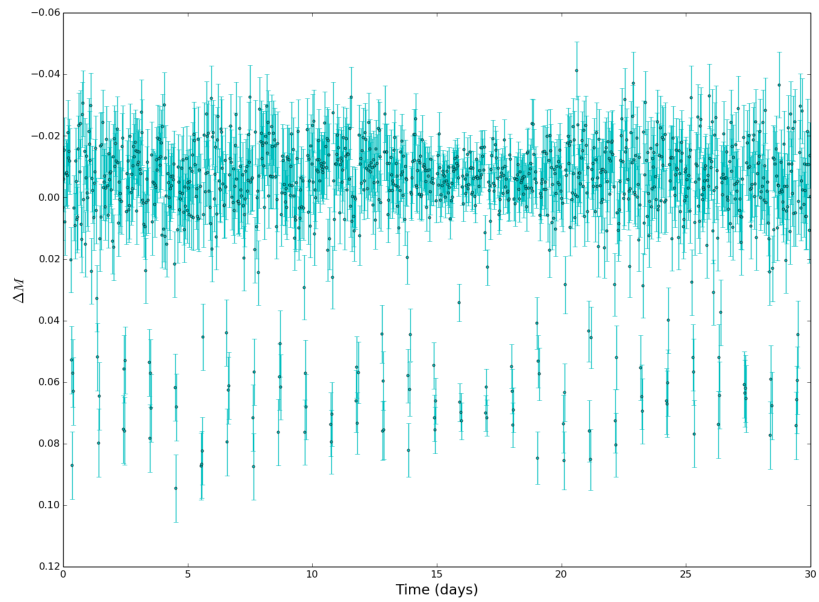

Figure 4.10: A residual transit light curve (with the microlensing fit subtracted off) with a period precision of 3% between the fitted and true period. The true period is 1.0 days and the star-planet radius ratio is $p = 0.26$.

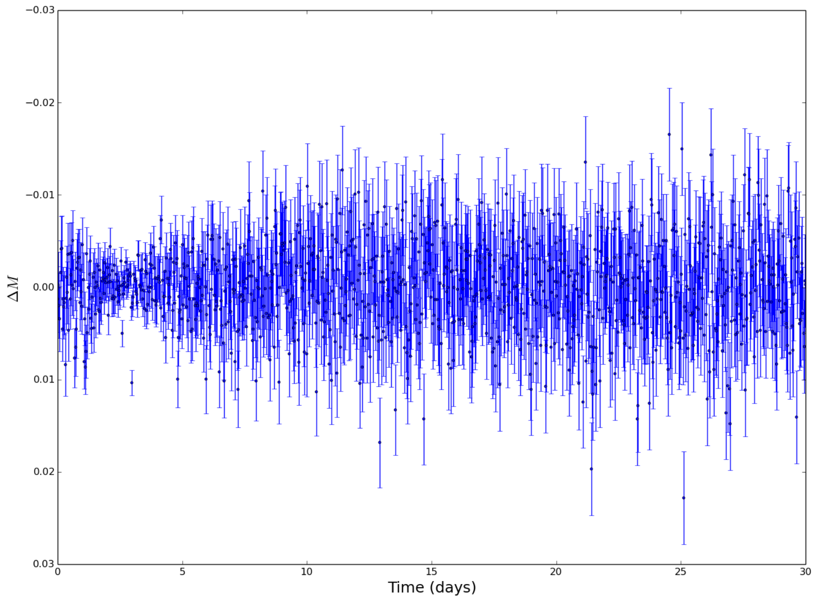

Figure 4.11: A residual transit light curve after subtracting the microlensing fit of a short duration event with $t_E = 5.2$ days. For clarity, only half of the number of points of the proposed ExELS survey are shown. Here, $t_0 = 2.8$ days, P=1.8 days, $u_0 = 0.07$ and $p = 0.1$.

source star, the microlensing event duration is an important factor because it determines the timescale over which the SNR of the transit signal can be improved by the microlensing effect. Figure 4.11, 4.12 and 4.13 are residual light curve examples (with the microlensing fit subtracted out) about the different values of t_E (representing examples of short, medium and long time scale events). For clarity, the plotted observation cadence is only half of the full ExELS's observing frequency.

4.3.2 The effect of transit duration on light curve quality

In order to detect transit signals, the transit duration time should be longer than the ExELS's proposed observation cadence (20 min). Figure 4.14, 4.15 and 4.16 show three examples of residual transit light curves with transit times that span the range of our simulation. For modest magnification events ($u_0 \sim 0.4$), transit depths from the folded transit light curves are not always clear however. As can be seen from the figures, a crucial determining factor is the planet-star radius fraction (p) which, if too small, leads to a transit signal which is too short to be seen with

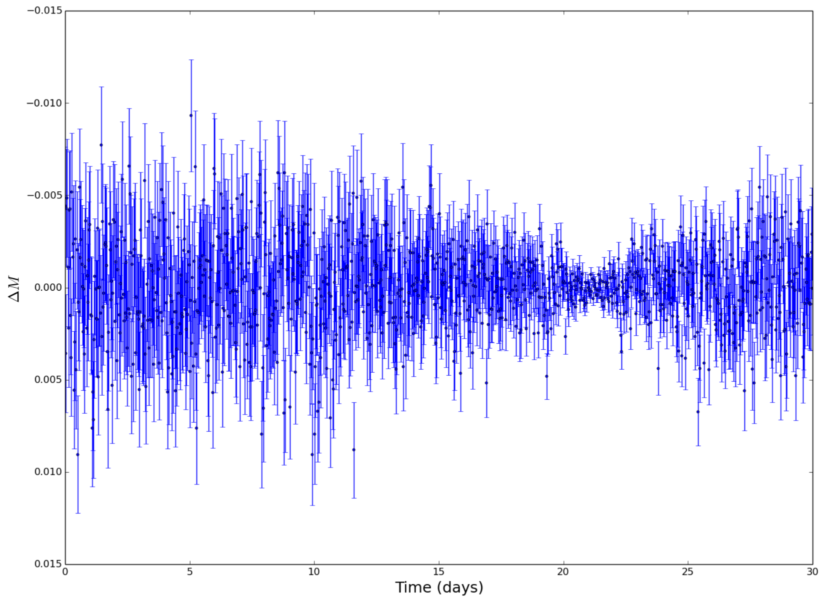

Figure 4.12: A residual transit light curve after subtracting the microlensing fit of a typical duration event with $t_E = 14.2$ days. For clarity, only half of the number of points of the proposed ExELS survey are shown. Here, the true parameter values are: $t_0 = 21.2$ days; P=6.1 days; $u_0 = 0.01$; and $p = 0.06$.

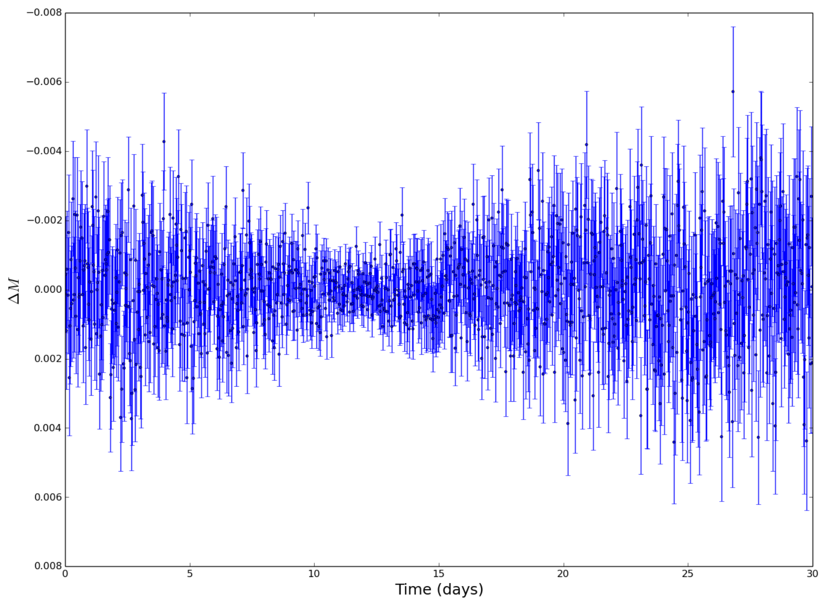

Figure 4.13: A residual transit light curve after subtracting the microlensing fit of a long duration event with $t_E = 23.3$ days. For clarity, only half of the number of points of the proposed ExELS survey are shown. Here, the true parameter values are: $t_0 = 11.5$ days; P=1.1 days; $u_0 = 0.05$; and $p = 0.08$.

Euclid's cadence. For clarity, the number of observation epochs in these figures is decreased by 2 times to 1080.

4.4 Microlensed transit detection fraction

We started this simulation with 9311 candidates generated from the Besançon Galactic model. 7339 candidates passed the SNR cut. After transit fitting with the `kepbls` routine in Section 3.7.1, we are left with 3082 candidates. Therefore, the proportion of detectable simulated event is $\sim 33\%$ under the assumption that every host star has one planet. However, not all simulated events are equally likely to be detectable as microlensing. To consider the overall detectability, we must weight our selection by the microlensing rate. We also need to allow for the fact that transit signals are only possible for restricted ranges of orbital inclination.

4.4.1 Microlensing event rate

The microlensing event rate for a particular source star at distance $D_s R$ can be expressed as (e.g. Paczynski, 1996b)

$$\Gamma(D_s) = \int_0^{D_s} \int_0^{\infty} R_E(D_l) V_t P(V_t, D_l) n(D_l) dV_t dD_l, \tag{4.1}$$

where D_l is the distance of the lensing star, R_E is the Einstein radius (Equation 1.5), V_t is the relative transverse velocity between the host (source) star and the lens star, $P(V_t, D_l)dV_t dD_l$ is the probability that the lens has relative velocity and distance in the range $[(V_t, V_t + dV_t), (D_l, D_l + dD_l)]$, and n is the volume number density of the lens stars at D_l. Since the Besanǫn Galactic model catalogue already provides stars drawn from model distributions of velocity, distance and magnitude, $P(V_t, D_l)$ is essentially already provided. The microlensing weighting for a particular source star j is therefore given by

$$W_j^{\mathrm{micro}} = \sum_{D_{l,i} < D_{s,j}} R_{E,ij} V_{t,ij} = \sum_{D_{l,i} < D_{s,j}} \mu_{\mathrm{rel},ij} D_{l,i}^2 \theta_{E,ij}, \tag{4.2}$$

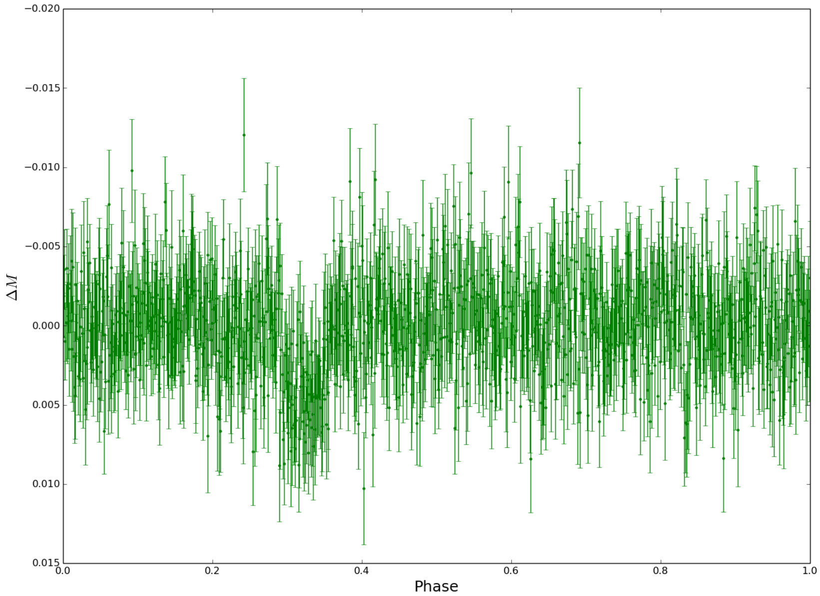

Figure 4.14: A residual folded transit light curve after subtracting the microlensing fit for a short duration transit with $t_{tran} = 0.08$ days. Here, $u_0 = 0.42$, true P=1.7 days and $p = 0.07$.

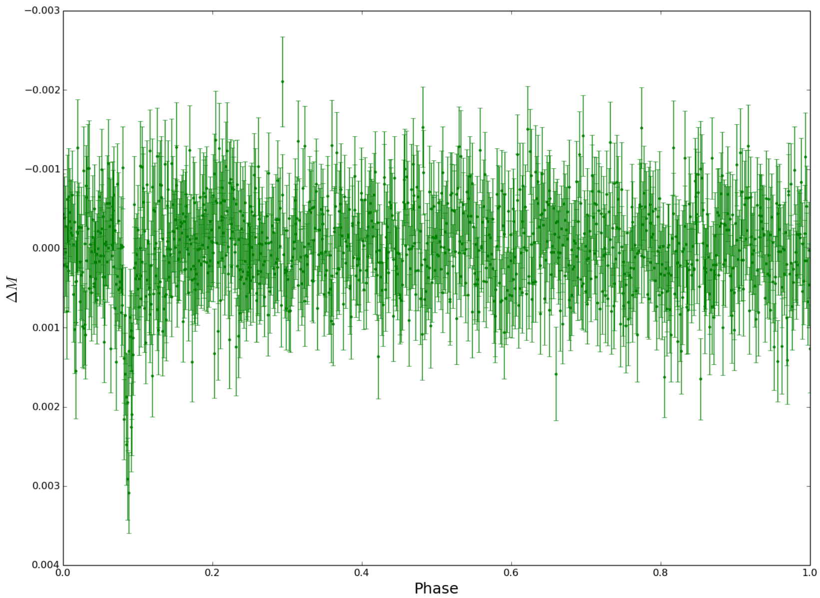

Figure 4.15: A residual folded transit light curve after subtracting the microlensing fit for a moderate duration transit with $t_{tran} = 0.28$ days. Here, $u_0 = 0.41$, true P=9.2 days and $p = 0.04$.

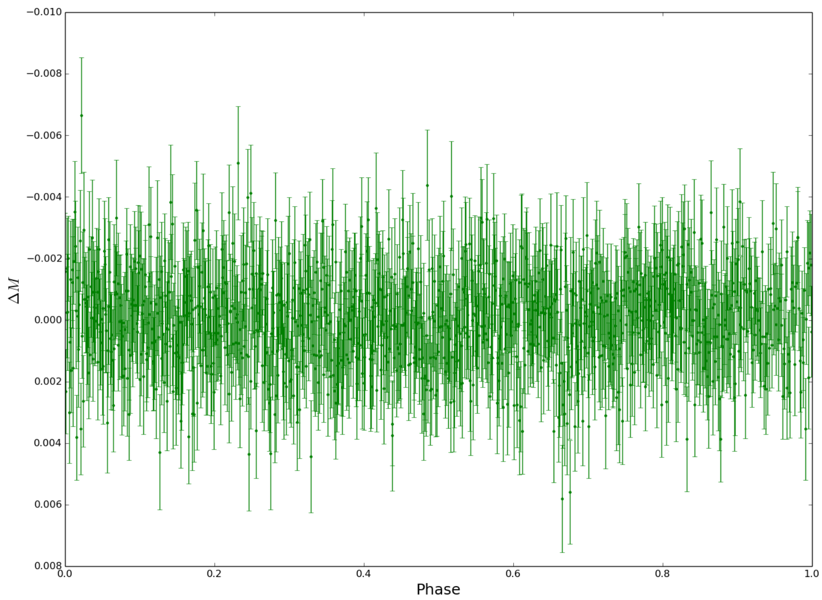

Figure 4.16: A residual folded transit light curve after subtracting the microlensing fit for a long duration transit with $t_{tran} = 0.44$ days. Here, $u_0 = 0.41$, true P=7.7 days and $p = 0.02$.

where subscript i refers to the lens, μ_{rel} is the lens relative proper motion and θ_E is the angular Einstein radius. The weights $W_j^{\rm micro}$ are pre-computed for the simulation.

4.4.2 Transit detectability

Since our simulation uses only inclination parameter which results in transit, we must weight for the fraction of orbital inclinations which yields transit signals. We therefore applied a weight

$$W_j^{\rm tran} = \frac{\pi/2 - i_{{\rm min},j}}{\pi/2}, \tag{4.3}$$

where $i_{\rm min}$ is the minimum inclination from Equation 3.10. The total detectability weight $W_j^{\rm tot} = W_j^{tran} \times W_j^{\rm micro}$.

The overall fraction of microlensing events with detectable transit signatures is therefore

$$f_{\rm detect} = \frac{\sum\limits_{i=1}^{N_{\rm detect}} W_i^{\rm tot}}{\sum\limits_{i=1}^{N_{\rm SNR}} W_i^{\rm tot}}, \tag{4.4}$$

where $N_{\mathrm{detect}} = 3082$ is the number of the simulated events which are successfully detected and $N_{\mathrm{SNR}} = 7339$ is the original number of simulated event which passed our SNR cut. The result of this equation is that $f_{\mathrm{detect}} = 0.18$. Penny et al. (2013) claim that ExELS should be capable of detecting 1,000 microlensing events per month. We should therefore expect it to find 180 microlensed transiting exoplanets if all microlensed source stars host one planet within the parameter range considered in our simulation.

4.5 Detectability versus the host star distance

Figure 4.17 shows the distance histogram of detectable microlensed transits. Since the Galactic bulge is located around 8 kpc, the highest detectability is expected there. However, some can be detected even behind the Galactic centre. There are more stars which can play a role of microlensing located at around 8 kpc from the observer than at closer distances. Microlensing can clearly help us to find exoplanets at greater distance that is found by traditional transit surveys (which have a range typically of a few kpc). The fact that microlensing can help to discover more distant exoplanet transit systems potentially means we can probe the affects of the Galactic environment on hot exoplanet statistics.

4.6 Detectability versus the host star magnitude

Figure 4.18 demonstrates the detectability with respect to the host stars' H-band magnitude. The purple histogram shows the microlensed H-band magnitude and the green one shows the baseline H-band magnitude, both from the finally selected candidates.

The reason for the rising trend from around 12 mag to 21 mag reflects the shape of the stellar luminosity function. The histogram shows that the majority of detectable host stars have a magnitude between roughly 17 mag to 22 mag. Beyond this limit, the numbers fall dramatically, reflecting the observational sensitivity limit of Euclid's

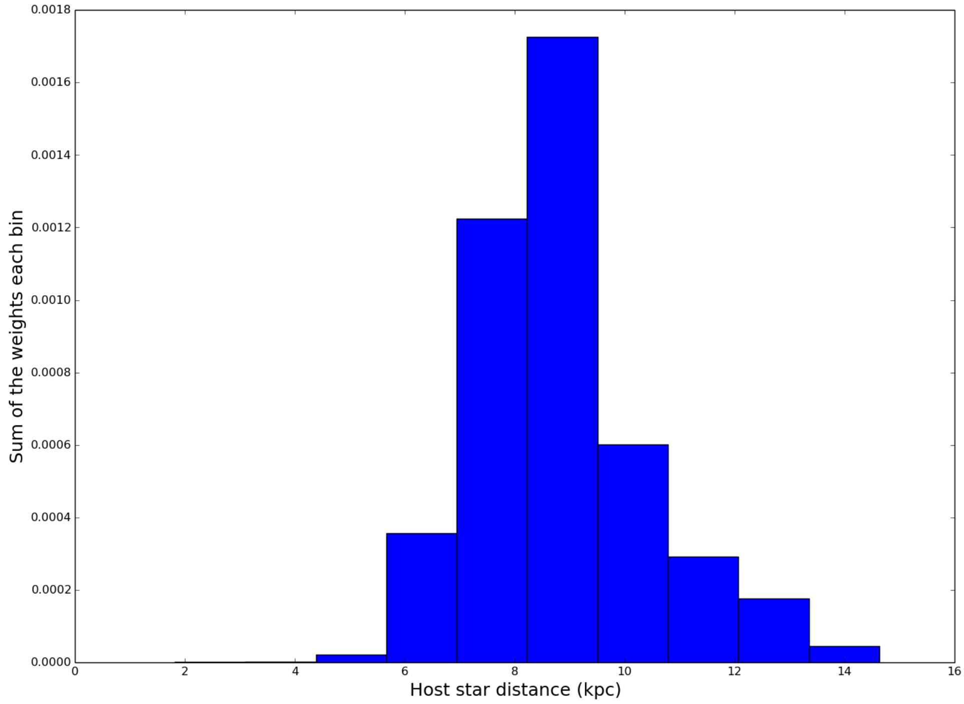

Figure 4.17: Histogram of host star distances. Weights on Y-axis refers a multiplication of W^{micro} and W^{tran}.

NISP instrument. The histogram of microlensed source star is approximately 2 mag brighter than the unlensed distribution. This indicates that microlensing typically provides a factor of ~ 6 increase in the number of photons from the source.

4.7 Detectability versus the Einstein time scale.

The distribution of weights with respect to the Einstein time scale (t_E) is shown in Figure 4.19 and largely follows the log-normal distribution of all microlensing events discussed in Equation 3.6, though with the tendency to peak at slightly longer durations. Approximately, 90% of sum-of-weights are located in the range between $ln(t_E/\mathrm{days}) = 1$ to 4.5 which is equivalent to $t_E = 2.7$ to 90 days. One noticeable point is that the value of weights are dramatically dropped when the transit weights are included (lower histogram).

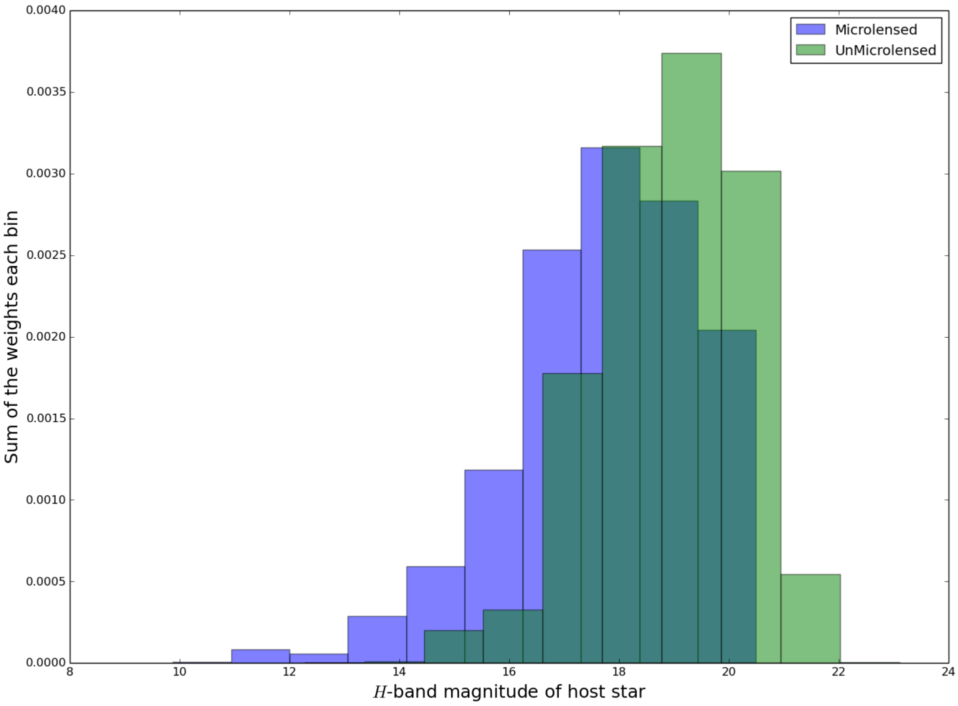

Figure 4.18: Histogram of the host stars baseline H-band magnitude (in green) from the finally selected candidates, together with the histogram of their peak magnitudes due to microlensing (in blue). Weights on Y-axis refers a multiplication of $W^{\rm micro}$ and $W^{\rm tran}$.

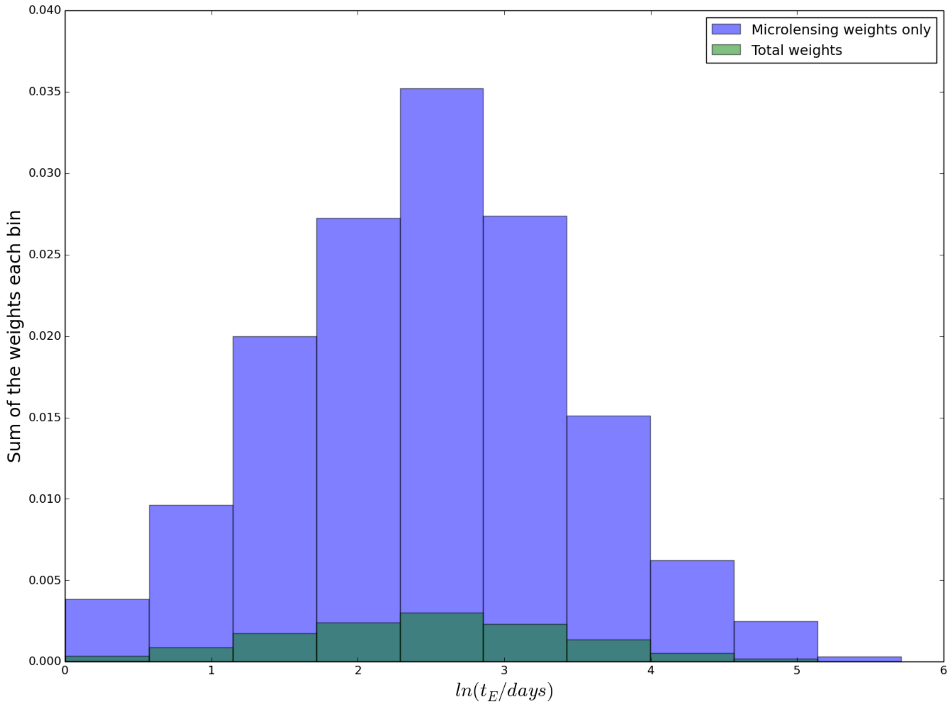

Figure 4.19: The histogram of weights W^{micro} (top) and W^{tot} (bottom) with respect to the Einstein time (t_E). Weights on Y-axis refers a multiplication of W^{micro} and W^{tran}.

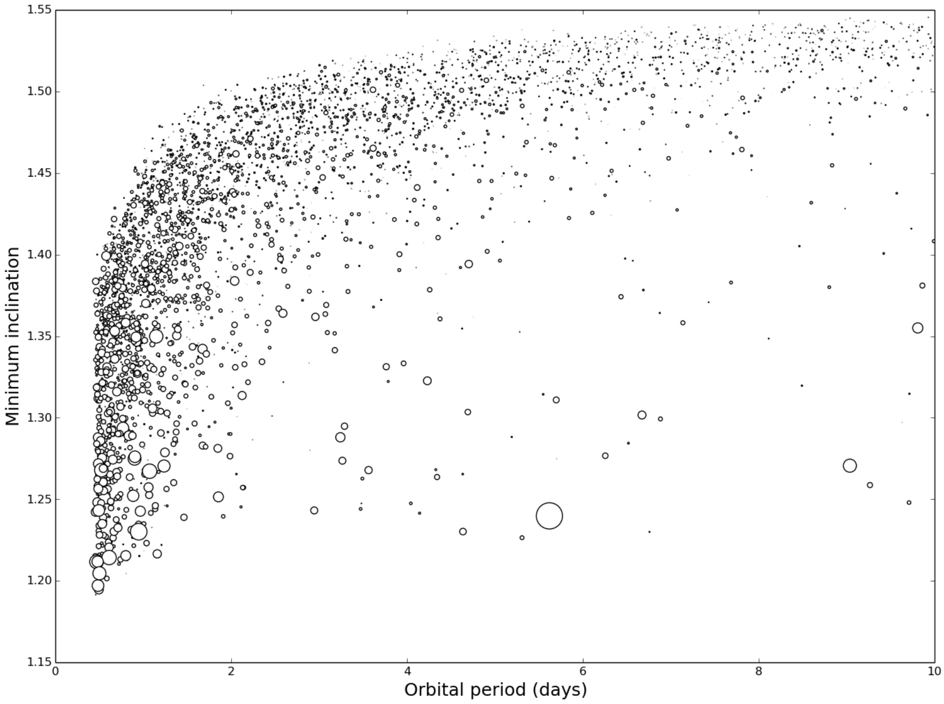

Figure 4.20: The relation between orbital period and minimum inclination. The circle radius is proportional to the total weight W^{tot}.

4.8 Detectability versus the orbital period and minimum inclination

As can be seen from Figure 4.20, according to the orbital period and minimum inclination, the distribution of weights has a general tendency towards lower periods and minimum inclination values, as expected. From Equation 3.10, the minimum inclination is strongly correlated with the planet-host separation and, hence the orbital period. Additionally, systems with low $i_{\min}$ have correspondingly larger W^{tran} from Equation 4.3. The correlation is not perfect however, because of the spread of simulated planet and star sizes.

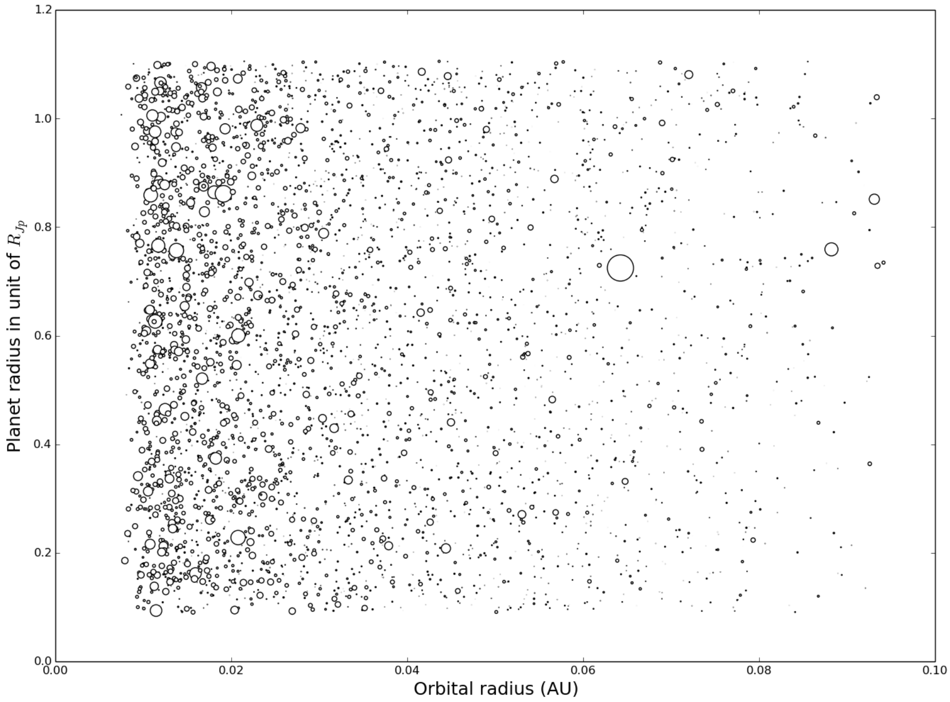

Figure 4.21: The relation between host separation and planet radius. Larger weights tend to occur at smaller host separation regardless of the planet size.

4.9 Detectability versus the orbital separation and planet radius

Figure 4.21 show a scatter plot of orbital separation versus planet radius for transiting systems which are detected in our simulation. From Equation 3.10 and 4.3, short host separation contributes to the high transit detectability for given radius of the star and the planet. However, as can be seen from the figure, these equations are not quite dependent on the size of planet. In most cases, the size of the planets are relatively very small compared to the size of their host stars even if the size of the planet is a Jupiter-sized. Therefore, no matter what their sizes are, a trend that a significant number of planets have higher weights at short orbital radius is shown in this figure and this indicates that host separation plays more important role than other variables in our transit detectability regime.

Chapter 5

Summary and further research

5.1 Research summary

We aimed to estimate the fraction of detectability for a rare type event, namely a microlensed transit signal, with Euclid's expected photometry. Firstly, we simulated microlensing and transiting events with randomly generated parameters within a specific range equating to the hot exoplanet regime. The Besanǫn Galactic model catalogue was also used to generate the host star properties. After generating light curves for this scenario, we introduced a cut in the signal-to-noise ratio for the detectable transit signals from a source star. After this process, 7339 candidates were selected as detectable from amongst 9311 initial candidates from the catalogue. Amongst these selected candidates, we performed a microlensing fit to the simulated data and validated the fitting method. Next, we subtracted off the microlensing fit and performed a transit period search on the residuals. We selected the subset which satisfied our period precision criteria. We used BLS fitting on the simulated residuals and the period precision criteria was applied in two steps to ensure accuracy at better than the 1% level.

The number of finally selected candidates was 3082. However, as discussed in Section 4.4, weights for the possible range of transit inclinations and for the microlensing event rate were also considered. After applying these weights, we obtained a detectable fraction of $f_{\mathrm{detect}} \sim 0.18$. The ExELS survey team anticipates finding around 1,000 microlensing events per month. If we apply our fraction onto the ExELS's expected microlensing event detection number, then we expect roughly 180 microlensed transit signals per month. This number is relatively high but assumes that every host star has at least one hot exoplanet within the size and host separation range we consider.

5.2 Avenues for further research

In chapter 3, we simulated transit and gravitational microlensing however, these scenarios need to be more precise. For instance, when it comes to the transit, eccentricity is needed for generating more realistic Keplerian orbit conditions. In addition, Limb darkening also needs to be considered for the same reason. Furthermore, there is also needed some improvements in the microlensing scenarios. As we simulated conditions that only one planet-source star system, in order to be seen more realistic, it is to be considered that binary and multiple planetary system as well in future work.

Our seclection criteria do not account for `kepbls` best fit solutions which are harmonics of the true periods. Such solutions should be regarded as detections but, we discard them as poorly determined periods. Further work on the selection algorithm could account for these cases. Therefore, generating more accurate and realistic simulations with these further considerations will be my future work.

Bibliography

Alibert Y., Baraffe I., Benz W., et al., 2006, A&A, 455, L25

Anderson D. R., Hellier C., Gillon M., et al., 2010, ApJ, 709, 159

Auvergne M., Bodin P., Boisnard L., et al., 2009, A&A, 506, 411

Bakos G., 2011, in Telescopes from Afar, edited by S. Gajadhar, J. Walawender, R. Genet, C. Veillet, A. Adamson, J. Martinez, J. Melnik, T. Jenness, N. Manset

Bakos G. Á., Hartman J. D., Torres G., et al., 2011, in European Physical Journal Web of Conferences, vol. 11 of European Physical Journal Web of Conferences, 1002

Barry R., Kruk J., Anderson J., et al., 2011, in Society of Photo-Optical Instrumentation Engineers (SPIE) Conference Series, vol. 8151 of Society of Photo-Optical Instrumentation Engineers (SPIE) Conference Series

Batalha N. M., 2014, Proceedings of the National Academy of Science, 111, 12647

Batalha N. M., Rowe J. F., Bryson S. T., et al., 2013, ApJS, 204, 24

Beaulieu J.-P., Bennett D. P., Fouqué P., et al., 2006, Nature, 439, 437

Beuermann K., Hessman F. V., Dreizler S., et al., 2010, A&A, 521, L60

Bodenheimer P., Pollack J. B., 1986, wecarus, 67, 391

Bond I. A., Udalski A., Jaroszyński M., et al., 2004a, ApJ, 606, L155

Bond I. A., Udalski A., Jaroszyński M., et al., 2004b, ApJ, 606, L155

Bonfils X., Forveille T., Delfosse X., et al., 2005, A&A, 443, L15

Borucki W. J., Koch D., Basri G., et al., 2010a, Science, 327, 977

Borucki W. J., Koch D., Basri G., et al., 2010b, Science, 327, 977

Borucki W. J., Koch D. G., Basri G., et al., 2011a, ApJ, 728, 117

Borucki W. J., Koch D. G., Basri G., et al., 2011b, ApJ, 736, 19

Bouchy F., Udry S., Mayor M., et al., 2005, A&A, 444, L15

Butler R. P., Marcy G. W., Fischer D. A., et al., 1999, ApJ, 526, 916

Butters O. W., West R. G., Anderson D. R., et al., 2010, A&A, 520, L10

Crampton D., Simard L., Silva D., 2009, TMT Science and Instruments, 279, Springer

Cumming A., Marcy G. W., Butler R. P., 1999, ApJ, 526, 890

Cutri R. M., Skrutskie M. F., van Dyk S., et al., 2003, VizieR Online Data Catalog, 2246, 0

de Bruijne J. H. J., 2012, Ap&SS, 341, 31

Deleuil M., Deeg H. J., Alonso R., et al., 2008, A&A, 491, 889

Dominik M., Albrow M. D., Beaulieu J.-P., et al., 2002, Planet. Space Sci., 50, 299

Dong S., DePoy D. L., Gaudi B. S., et al., 2006a, ApJ, 642, 842

Dong S., DePoy D. L., Gaudi B. S., Gould A., et al., 2006b, ApJ, 642, 842

Ehrenreich D., Lecavelier des Etangs A., Beaulieu J.-P., Grasset O., 2006, ApJ, 651, 535

Einasto J., 1979, in The Large-Scale Characteristics of the Galaxy, edited by W. B. Burton, vol. 84 of IAU Symposium, 451–458

European Southern Observatory, 2005, in European Southern Observatory Press Release, 12

Gaudi B. S., 2012, ARA&A, 50, 411

Hatzes A. P., Cochran W. D., Endl M., et al., 2003, ApJ, 599, 1383

Haywood M., Robin A. C., Creze M., 1997, A&A, 320, 440

Hubickyj O., Bodenheimer P., Lissauer J. J., 2004, in Revista Mexicana de Astronomia y Astrofisica Conference Series, edited by G. Garcia-Segura, G. Tenorio-Tagle, J. Franco, H. W. Yorke, vol. 22 of Revista Mexicana de Astronomia y Astrofisica Conference Series, 83–86

Ida S., Lin D. N. C., 2005, ApJ, 626, 1045

Jahreiß H., Wielen R., 1997, in Hipparcos - Venice '97, edited by R. M. Bonnet, E. Høg, P. L. Bernacca, L. Emiliani, A. Blaauw, C. Turon, J. Kovalevsky, L. Lindegren, H. Hassan, M. Bouffard, B. Strim, D. Heger, M. A. C. Perryman, L. Woltjer, vol. 402 of ESA Special Publication, 675–680

Jetzer P., 1999, in 3K cosmology, edited by L. Maiani, F. Melchiorri, N. Vittorio, vol. 476 of American Institute of Physics Conference Series, 135–148

Johns M., 2008, in Society of Photo-Optical Instrumentation Engineers (SPIE) Conference Series, vol. 6986

Kalas P., Graham J. R., Chiang E., et al., 2008, Science, 322, 1345

Kennedy G. M., Kenyon S. J., 2008, ApJ, 682, 1264

Kim S.-L., Park B.-G., Lee C.-U., et al., 2010, in Society of Photo-Optical Instrumentation Engineers (SPIE) Conference Series, vol. 7733 of Society of Photo-Optical Instrumentation Engineers (SPIE) Conference Series

Kovács G., Zucker S., Mazeh T., 2002, A&A, 391, 369

Laureijs R., Amiaux J., Arduini S., et al., 2011, ArXiv e-prints, 1100.3193L

Laureijs R., Gondoin P., Duvet L., et al., 2012, in Society of Photo-Optical Instrumentation Engineers (SPIE) Conference Series, vol. 8442 of Society of Photo-Optical Instrumentation Engineers (SPIE) Conference Series, 0

Laureijs R., Hoar J., Buenadicha G., et al., 2014, in Astronomical Society of the Pacific Conference Series, edited by N. Manset, P. Forshay, vol. 485 of Astronomical Society of the Pacific Conference Series, 495

Lee J. W., Kim S.-L., Kim C.-H., et al., 2009, AJ, 137, 3181

Léger A., Rouan D., Schneider J., et al., 2009, A&A, 506, 287

Mandel K., Agol E., 2002, ApJ, 580, L171

Mao S., Paczynski B., 1991, ApJ, 374, L37

Marchiori G., Busatta A., Ghedin L., De Lorenzi S., 2012, in Society of Photo-Optical Instrumentation Engineers (SPIE) Conference Series, vol. 8444 of Society of Photo-Optical Instrumentation Engineers (SPIE) Conference Series

Marshall D. J., Robin A. C., Reylé C., Schultheis M., Picaud S., 2006, A&A, 453, 635

Mayor M., Queloz D., 1995, Nature, 378, 355

Murray C. D., Correia A. C. M., 2011, Keplerian Orbits and Dynamics of Exoplanets, 15–23

Paczynski B., 1996a, ARA&A, 34, 419

Paczynski B., 1996b, ARA&A, 34, 419

Penny M. T., Kerins E., Rattenbury N., et al., 2013, MNRAS, 434, 2

Perryman M., 2011, The Exoplanet Handbook, Cambridge University Press

Picaud S., Robin A. C., 2004, A&A, 428, 891

Pollacco D. L., Skillen I., Collier Cameron A., et al., 2006, PASP, 118, 1407

Qian S.-B., Liao W.-P., Zhu L.-Y., Dai Z.-B., 2010, ApJ, 708, L66

Queloz D., Eggenberger A., Mayor M., et al., 2000, A&A, 359, L13

Rauer H., Catala C., Aerts C., et al., 2014, Experimental Astronomy

Robin A. C., Marshall D. J., Schultheis M., Reylé C., 2012, A&A, 538, A106

Robin A. C., Reylé C., Derrière S., Picaud S., 2003, A&A, 409, 523

Sing D. K., Lecavelier des Etangs A., Fortney J. J., et al., 2013, MNRAS, 436, 2956

Sipőcz B., Kovács G., Hodgkin S., Pinfield D., 2013, in European Physical Journal Web of Conferences, vol. 47 of European Physical Journal Web of Conferences, 1001

Smith A. M. S., WASP Consortium, 2014, Contributions of the Astronomical Observatory Skalnate Pleso, 43, 500

Sozzetti A., 2014, ArXiv e-prints, 1406.1388S

Still M., Barclay T., 2012, PyKE: Reduction and analysis of Kepler Simple Aperture Photometry data, Astrophysics Source Code Library

Sumi T., 2010, in Pathways Towards Habitable Planets, edited by V. Coudé du Foresto, D. M. Gelino, I. Ribas, vol. 430 of Astronomical Society of the Pacific Conference Series, 225

Sumi T., Kamiya K., Bennett D. P., et al., 2011, Nature, 473, 349

Udalski A., 2003, Acta Astron., 53, 291

Udalski A., Jaroszyński M., Paczyński B., et al., 2005, ApJ, 628, L109

Udalski A., Szymanski M., Mao S., et al., 1994, ApJ, 436, L103

Welsh W. F., Orosz J. A., Seager S., et al., 2010, ApJ, 713, L145

Winn J. N., 2010, ArXiv e-prints, 1001,2010W

Wolszczan A., Frail D. A., 1992, Nature, 355, 145

Wyrzykowski L., Rynkiewicz A. E., Skowron J., et al., 2014, ArXiv e-prints, 1405.3134W

Yock P., Bond I., Rattenbury N., et al., 2000, ArXiv Astrophysics e-prints, 007317

Appendix A

Program

```
#Author: Yun-Hak Kim (yousung30905@gmail.com, yun-hak.kim@postgrad.manchester.ac.uk)
#Project: The detectability of transit signals from a microlensed source star with Euclid
#University: University of Manchester
#Degree: M.Phil (Astronomy and Astrophysics)
#Programming language: Python 2.7.5 and Pyraf

import numpy as np
np.set_printoptions(threshold=np.nan)
import scipy as sp
from scipy import optimize
from scipy.optimize import leastsq
import matplotlib.pyplot as plt
import sys
from pyraf import iraf
import pyfits as pf
iraf.kepler(_doprint=0)

#Defining Magnification depends on time
def a(v,t):
    return (v[1]**2+((t-v[2])/v[3])**2+2.0) / ((np.sqrt(v[1]**2+((t-v[2])/v[3])**2))*(np.sqrt(v[1]**2+((t-v[2])/v[3])**2+4.0)))

#Mandel&Agol 2002 model
def L(t,z,sizefrac,Period,frac,phi):
    ans = -9999.0
    ans = np.where(1.0+sizefrac<z, 0., ans)
    ans = np.where(np.logical_and(np.abs(1.0-sizefrac<z),1.0+sizefrac>=z), frac, ans)
    ans = np.where(z<=1.0-sizefrac, sizefrac**2, ans)
    ans = np.where(np.mod(t+((Period*phi)/360.0),Period)>=(Period/2.0), 0., ans)
        return 1.0-ans

#Opening Besançon Galactic model catalogue and extract parameters (H-band magnitude, Mass
```

of a star, Radius of a star and Distance from the observer)

file1 = open("yun.res", 'r')

file1.close()

data1,data2,data3,data4 = np.genfromtxt("yun.res", skip_header=114, skip_footer=1, usecols=(0,23,25,31), unpack = True)

#Opening microlensing weight file

file2 = open("yun-weights.dat", 'r')

file2.close()

#Giving ID number for every candidates from the catalogue

ID = np.arange(len(data1))

#Generating random microlensing impact parameter u_0

u0 = 0.999*np.random.random(len(data1))+0.001

#Generating Peak magnification A_0 corresponds to u_0

A0 = (u0**2 +2.0) / (u0*np.sqrt(u0**2+4.0))

#Euclid's photometry from Table 3.1

texpH = 54.0

MagABH = 24.92

MagBGH = 21.4

aperture = 0.9

#Magnitude within the aperture

MagAP = MagBGH - 2.5*np.log10(np.pi*aperture**2 / 4.0)

#Number of photons from a background within the aperture

n_bg = 10**(0.4*(MagABH-MagAP))

#Number of photons from a source star

n_ps = 10**(0.4*(MagABH-data1))

#Observing duration and its cadence

t = np.linspace(0.0, 30.0,2160.0)

#Generating random t_0

t_0 = np.random.random(len(data1))*30.0

#Logarithmic mean value of Einstein radius crossing time t_E

meantE = 2.5

#standard deviation of Einstein radius crossing time t_E

sigtE = 1.0

```
#Generating random Einstein radius crossing time t_E
lnt_E = np.abs(sigtE * np.random.randn(len(data1)) + meantE)
t_E = np.abs(np.exp(lnt_E))

#Gravitational constant in units of (AU^3/M(sun) * yr^2)
G = 4.0*(np.pi**2.0)
#Making a constant for converting AU to the Solar radius unit
convert = ((1.496 / 6.96)*(10.0**3.0))

#Minimum host separation in units of AU
Omin = (3.0*data3)*(1.0/convert)

#Maximum host separation in units of AU
Omax = ((((10.0/365.0)**2)*data2)**(1.0/3.0))

#Deviation of the logarithmic host separation
lnminus = np.log(Omax)-np.log(Omin)

#Generating random host separation range
R = np.exp(lnminus*np.random.random(len(data1))+np.log(Omin))

#Host separation in units of the Solar radius
OR = R * convert

#Generating angle phase of an exoplanet orbit for transit (0~2pi)
angle = 360.0*np.random.random(len(data1))

#Exoplanet Size from Earth-sized (0.009) to Jupiter-sized (0.11) normalized by the Solar radius
sizefrac1 = (0.101*np.random.random(len(data1))+0.009)

#Size fraction between exoplanet and star
sizefrac = sizefrac1 / data3

#Equation for signal-to-noise ratio
SN = (n_ps*texpH*A0) / (np.sqrt((n_bg*texpH)+(n_ps*texpH*A0)))

#Adjusting the cut line
cut11 = np.logical_and((SN>=50.0),(Omax>Omin))
Enough00= np.where(cut11)
Enough0= np.asarray(Enough00)
Enough = np.where(np.logical_and(cut11,(0.55*period)>0.251))

#Parameters selection
Hdetect = data1[Enough]
```

Rdetect = data3[Enough]

Mdetect = data2[Enough]

u0detect = u0[Enough]

t_0detect = t_0[Enough]

t_Edetect = np.abs(t_E[Enough])

Pdetect = period[Enough]

ordetect = OR[Enough]

Angledetect = angle[Enough]

SPdetect = sizefrac1[Enough]

SFdetect = sizefrac[Enough]

n_psdetect = n_ps[Enough]

IDdetect = ID[Enough]

WTdetect = data5[Enough]

Disdetect= data4[Enough]

#Generating void list for each selected parameters

pp1=[]

iddl=[]

hmagl1=[]

uzl1=[]

tzl1=[]

teel1=[]

Mdl1=[]

rdl1=[]

Ordl1=[]

pedl1=[]

angl1=[]

spdl1=[]

sfdl1=[]

WINC=[]

inc1=[]

incmin1=[]

DIS=[]

Trandu=[]

NPS1=[]

WINC=[]

WML=[]

idfinal=[]

Tran=[]

#Zipping together

sel = zip(Hdetect,Mdetect,Rdetect,u0detect,t_0detect,t_Edetect,Pdetect,ordetect,Angledetect,SPdetect,SFdetect,n_psdetect ,IDdetect,WTdetect,Disdetect)

#Generating `for` loop

```
for hmag,Md,rd,uz,tz,tee,ped,Ord,ang,spd,sfd,nps,idd,WT,dis in sel:
#Generating horizontal component of z from Equation 3.9
    zl = np.abs(Ord*np.cos((2.0*np.pi*t / ped) + ang))
#Sum of star's radius and planet's radius for a minimum inclination
    smax=rd+spd
    imin=np.arccos(smax/Ord)
#Generating inclination
    i=((np.pi/2.0)-imin)*np.random.random()+imin
#Generating vertical component of z from Equation 3.11
    zs = Ord*np.cos(i)
#Generating transiting weights
    winc=((np.pi/2.0)-imin)/(np.pi/2.0)
#Generating a two-dimensional z
    Z=np.sqrt((zl**2)+(zs**2))
#Parameters for Mandel&Agol 2002 model
    k0 = np.arccos((sfd**2+Z**2-1.0)/(2.0*sfd*Z))
    k1 = np.arccos((1.0-sfd**2+Z**2)/(2.0*Z))
    f = (4.0*Z**2-(1.0+Z**2-sfd**2)**2)/4.0
    Frac = (sfd**2*k0+k1-np.sqrt(f))/ np.pi
#Calculating a transit duration by Eq 3.18
    trandu=(ped/np.pi)*np.arcsin((rd/Ord)*(np.sqrt((1+sfd)**2-zs**2)/np.sin(i)))
#Binding the microlensing parameters
    v=[hmag,uz,tz,tee]
#Generate a data light curve
    M1 = v[0]-2.5*np.log10(a(v,t)*L(t,Z,sfd,ped,Frac,ang))
#Extract photon noise from the signal to noise ratio equation
    noise = np.sqrt((n_bg*texpH)+(nps*texpH*a(v,t)*L(t,Z,sfd,ped,Frac,ang)))
#Initiall guesses
    Hguess = np.median(M1)
    u0guess = 10.0**(-0.4*(np.max(M1)-np.min(M1)))
    t0guess = t[np.argwhere(M1==np.min(M1))]
    tEguess = np.exp(meantE)
#Binding them
    v0 = [Hguess,u0guess,t0guess,tEguess]
#Generating δM
    ER = (1.0 / noise) * (2.5 / np.log(10.0))
#Generating a realized data light curve with the ER
    Mdata = np.random.normal(M1,ER)
#Generating a model microlensing light curve
    Mmodel = lambda v,t: v[0]-2.5*np.log10(a(v,t))
#χ square
    e = lambda v,t,Mdata: (Mdata-Mmodel(v,t)) / ER
#Fitting
    v1 = sp.optimize.leastsq(e,v0,args=(t,Mdata),full_output=1,maxfev=10000)
#Changing name of Mdata and generating a model microlensing light curve with fitted parameters
```

```
    y2 = Mdata
    y3 = lambda v1,t: v1[0][0]-2.5*np.log10((v1[0][1]**2+((t-v1[0][2])/v1[0][3])**2+2.0) / ((np.sqrt(v1[0][1]**2+((t-
v1[0][2])/v1[0][3])**2))*(np.sqrt(v1[0][1]**2+((t-v1[0][2])/v1[0][3])**2+4.0))))
#Extracting transit signals
    y4 = y2-y3(v1,t)
#Converting to FITS file type
    np.savetxt("Subvalues.txt",np.transpose((t,y4,ER)))
    iraf.kepconvert(infile='Subvalues.txt',outfile='Subconverted.fits',conversion='asc2fits',columns='TIME,RAW_FLUX,
RAW_FLUX_ERR',clobber='y')
#Period process using kepbls routine for a crude search
    iraf.kepbls(infile='Subconverted.fits',outfile='kpblsoutput.fits',datacol='RAW_FLUX',errcol='RAW_FLUX_ERR',
minper=0.55*ped,maxper=1.95*ped,mindur=1.0,maxdur=12,nsearch=100,nbins=100,plot='n',clobber='y')
#Extracting the most preferrable trial period from the crude search routine
    fits=pf.open('kpblsoutput.fits')
    fitsdata=fits[2].header
    periodfits=fitsdata['PERIOD']
#Cacluating period fraction
    wow = np.abs((periodfits - ped) / ped)
#Period process using kepbls routine for a more precised search
    if wow <= 1.4/100.0:
        iraf.kepbls(infile='Subconverted.fits',outfile='kpblsoutput2.fits'
,datacol='RAW_FLUX',errcol='RAW_FLUX_ERR',minper=0.97*ped,maxper=1.03*ped,mindur=1.2,
maxdur=11,nsearch=100,nbins=30,plot='n',clobber='y')
#Extracting the most preferrable trial period from the more precised search routine
        fits2=pf.open('kpblsoutput2.fits')
        fitsdata2=fits[2].header
        periodfits2=fitsdata['PERIOD']
#Cacluating period fraction
        wowwow = np.abs((periodfits2 - ped) / ped)
#Final selection
        if wowwow < 0.01:
            idfinal.append(idd)

#Generating catalogue for selected parameters
np.savetxt("Tableforall.txt",np.transpose((iddl,pp1,hmagl1,uzl1,tzl1,teel1,Mdl1,rdl1,Ordl1,pedl1,Tran,angl1,spdl1,sfdl1,inc1,
incmin1,NPS1,WINC,WML,DIS)))
np.savetxt("finalIDtable.txt",np.transpose(idfinal))
```